



# Correlation times of velocity and kinetic helicity fluctuations in non-helical hydrodynamic turbulence

Hongzhe Zhou<sup>1,2,†</sup> and Naveen Jingade<sup>3,†</sup>

<sup>1</sup>Tsung-Dao Lee Institute, Shanghai Jiao Tong University, Shanghai 201210, PR China

<sup>2</sup>Nordita, KTH Royal Institute of Technology and Stockholm University, Hannes Alfvéns väg 12, SE-106 91 Stockholm, Sweden

<sup>3</sup>Indian Institute of Astrophysics, Koramangala, Bengaluru 560034, India

(Received 8 February 2024; revised 8 September 2024; accepted 11 October 2024)

Non-helical turbulence within a linear shear flow has demonstrated efficient amplification of large-scale magnetic fields in numerical simulations, but its precise mechanism remains elusive. The incoherent  $\alpha$  mechanism proposes that a zero-mean fluctuating transport coefficient  $\alpha$  (linked to kinetic helicity) in the shear flow is a candidate driver. Previous renovating-flow models have proposed that the correlation time of helicity fluctuations must be sufficiently extended to overcome turbulent magnetic diffusivity, yet only empirical validation of this concept has been obtained. In this study, we conduct direct numerical simulations of weakly compressible non-helical hydrodynamic turbulence. We scrutinize the correlation times of velocity and kinetic helicity fluctuations in distinct flow configurations, including rotation, shearing and Keplerian flows, as well as the shearing turbulence counterpart. Our findings indicate that rotation contributes to a prolonged correlation time of helicity compared with velocity, particularly notable in auto-correlations of both volume-averaged quantities and individual Fourier modes due to the formation of large-scale vortices. In contrast, moderate shear strength does not exhibit significant scale separation, with shear flows elongating vortices in the shear direction. Shearing turbulence, characterized by shorter helicity correlation times, appears less conducive to hosting the incoherent  $\alpha$  effect. Notably, at modest shear rates, only Keplerian flows exhibit sufficiently coherent helicity fluctuations, in contrast to shearing flows. However, the relative strength of helicity fluctuations compared with turbulent diffusivity is significantly lower, raising doubts about the viability of the incoherent  $\alpha$  effect as a potential dynamo driver in the subsonic flows examined in this study.

† Email addresses for correspondence: [hongzhe.zhou@sjtu.edu.cn](mailto:hongzhe.zhou@sjtu.edu.cn), [naveen.jingade@iiap.res.in](mailto:naveen.jingade@iiap.res.in)

© The Author(s), 2024. Published by Cambridge University Press. This is an Open Access article, distributed under the terms of the Creative Commons Attribution licence (<http://creativecommons.org/licenses/by/4.0/>), which permits unrestricted re-use, distribution and reproduction, provided the original article is properly cited.

**Key words:** dynamo theory, rotating turbulence, turbulence simulation

## 1. Introduction

Magnetic fields in astrophysical systems, encompassing celestial bodies such as stars, galaxies and accretion disks, necessitate sustained mechanisms for their persistence against the effects of microphysical dissipation, a role aptly fulfilled by dynamos. The study of magnetic field evolution, especially on scales exceeding the outer scale of turbulence, is conventionally approached through the prism of large-scale or mean-field dynamo theories (Steenbeck, Krause & Rädler 1966). A fundamental driver in mean-field dynamos is the net kinetic helicity intrinsic to the flow (Parker 1955) which naturally emerges in the presence of rotation and density stratification, commonly encapsulated in the  $\alpha$  effect. In this context, the mean-field dynamo coefficient  $\alpha$  intricately depends on the product of kinetic helicity and the eddy turnover time.

The last two decades have witnessed the recognition of a novel class of mean-field dynamos that operates without the need for a net kinetic helicity. Instead, a background shear flow coupled with non-helical turbulence, is deemed sufficient (Brandenburg 2005; Yousef *et al.* 2008). A leading theoretical framework to explain this phenomenon is the shear-current effect (Rogachevskii & Kleeorin 2003, 2004; Rädler & Stepanov 2006; Rüdiger & Kitchatinov 2006; Pipin 2008; Sridhar & Subramanian 2009a; Sridhar & Singh 2010; Singh & Sridhar 2011; Squire & Bhattacharjee 2015b; Zhou & Blackman 2021; Skoutnev, Squire & Bhattacharjee 2022), which postulates a dynamo driver rooted in an anisotropic turbulent magnetic diffusivity tensor.

While the shear-current effect has been theorized to exist, its numerical substantiation has been a subject of debate (Brandenburg *et al.* 2008; Squire & Bhattacharjee 2015a,c, 2016; Käpylä *et al.* 2020; Käpylä, Rheinhardt & Brandenburg 2022). An alternative theoretical approach to addressing the shear dynamo problem is the incoherent  $\alpha$  effect, wherein the interplay of shear and a fluctuating  $\alpha$  coefficient with a zero mean is considered. The concept of incoherent  $\alpha$  entering the mean-field induction equation dates back to the seminal works by Kraichnan (1976) and Moffatt (1978), who demonstrated that  $\alpha$  fluctuations can effectively act as a negative turbulent diffusivity and contribute as an effective drift velocity if they are statistically inhomogeneous, especially when  $\alpha$  fluctuations are delta correlated. For dynamo action to occur, it is crucial that the fluctuations are strong and coherent enough, satisfying  $\tau_\alpha \alpha_{rms}^2 \gtrsim \beta$ , where  $\tau_\alpha$  is the correlation time,  $\alpha_{rms}$  is the root-mean-square (r.m.s.) amplitude of  $\alpha$  fluctuations and  $\beta$  represents the turbulent diffusivity (Kraichnan 1976).

In a related study (Jingade, Singh & Sridhar 2018), the authors extended the work of Kraichnan (1976) to include non-zero correlation times for  $\alpha$  fluctuations in the presence of a background shear flow. The study showed that dynamo action is possible when there are large-scale spatial inhomogeneities in the amplitudes of the  $\alpha$  fluctuations. The validity of this result in the doubly averaged mean field depends on the time-scale separation between velocity fluctuations and  $\alpha$  fluctuations, and we aim to explore and elaborate on this aspect in the present work.

In light of the limitations of Jingade *et al.* (2018), which work is confined to small correlation times, the work of Jingade *et al.* (2018) was further extended to arbitrary correlation times for the velocity field using renovating flows (Gilbert & Bayly 1992), taking into account the background shear self-consistently. Jingade & Singh (2021) explored helicity fluctuations of the random velocity fields, also considering the idea

that helicity can be correlated over times much larger than the correlation time of the velocity field, following the propositions of Kraichnan (1976) and Sokolov (1997). The main objective of this extended study was to demonstrate that large-scale dynamo action is possible when there is such time-scale separation between helicity fluctuations and velocity fluctuations, in the absence of negative diffusion (in this work, by ‘scale separation’ we always refer to the case where the correlation time of the helicity fluctuations is much longer than that of the velocity fluctuations, although the opposite case exhibits separated time scales as well, since only the former is relevant to mean-field dynamo theories). This emphasizes the significance of scale separation, a factor often overlooked in papers on mean-field electrodynamics with  $\alpha$  (helicity) fluctuations and scarcely measured in numerical simulations. Additionally, through the application of the renovating-flow model in a shear flow, Jingade & Singh (2021) identified a critical condition for mean-field dynamo action, stipulating that  $\tau_h/\tau_u > 3$ , where  $\tau_u$  represents the correlation time of the turbulent velocity field, and  $\tau_h$  represents correlation time of helicity fluctuations. It is crucial to highlight that this conclusion was drawn from considering a single-scale flow model. In this study, we go beyond the single-scale model and aim to explore whether large-scale flow phenomena such as shear or rotation induce a time-scale separation between velocity and helicity fluctuations in direct numerical simulations of hydrodynamical turbulence.

The possibility of a shear dynamo driven by a stochastic  $\alpha$  has also been demonstrated by directly solving for the large-scale magnetic field or its second-order moment, without explicitly deriving the contribution of  $\alpha_{rms}$  to the turbulent electromotive force (Vishniac & Brandenburg 1997; Fedotov, Bashkirtseva & Ryashko 2006; Proctor 2007; Heinemann, McWilliams & Schekochihin 2011; Mitra & Brandenburg 2012; Richardson & Proctor 2012). The impact of an additional stochastic component on the conventional  $\alpha$  effect has been explored by Newton & Kim (2012) in the context of the solar dynamo. Moreover, Sur & Subramanian (2009) suggested that a fluctuating  $\alpha$  might help mitigate the catastrophic quenching in the absence of a helicity flux.

In the aforementioned studies,  $\alpha$  fluctuations are often prescribed (e.g. as white noise with a given amplitude or as finite correlated noise), but the origin of such fluctuations is not explicitly demonstrated. One potential source of these fluctuations arises from the violation of the Reynolds-averaging rules (Hoyng 1987). Alternatively, Kraichnan (1976), Moffatt (1978) and Kleeorin & Rogachevskii (2008) attribute them to the intrinsic fluctuations of the turbulent flow.

The task of determining turbulent transport coefficients in simulations is significantly facilitated by the test-field method (Brandenburg *et al.* 2008; Rheinhardt & Brandenburg 2010; Käpylä *et al.* 2020, 2022). Brandenburg *et al.* (2008) observed that, in shearing turbulence, all components of the  $\alpha$  tensor undergo random fluctuations, following a Gaussian distribution. The amplitude  $\alpha_{rms}$ , normalized by  $\beta$  and the forcing wavenumber  $k_f$ , increases with an increasing magnetic Reynolds number  $Rm$  and saturates at  $Rm = 10$ . However, it shows a relatively weak dependence on the shear rate at Reynolds and magnetic Reynolds numbers  $\lesssim O(10)$ . It is worth noting that the correlation time of  $\alpha$  fluctuations was not addressed in their study, and this is precisely the focus of the present work.

In this study, we aim to ascertain the correlation times of velocity and kinetic helicity directly from their time series in numerical simulations, and determine whether the correlation time of helicity fluctuations can exceed that of the velocity fluctuations in various cases. We focus on the kinematic phase of the shear dynamo problem, i.e. when the Lorentz back reaction is negligible in the Navier–Stokes equation. The subsequent sections are organized as follows: § 2 briefly introduces the mean-field dynamo formalism and the

$\alpha$  fluctuations. In § 3, we provide essential definitions of two-point correlators and describe the simulation set-ups. Sections 4 and 5 delve into the investigation of turbulent velocity and helicity correlation times under rotating and shearing background flows, respectively. Section 6 discusses the implications of our findings and relates them to previous shear dynamo simulations. Finally, we present a summary of our findings in § 7.

## 2. Background

### 2.1. Mean-field setting: $\alpha$ -fluctuations

The evolution of the magnetic field in magnetohydrodynamics is described by the induction equation, which, in the non-relativistic limit, can be expressed as

$$\frac{\partial \mathbf{B}}{\partial t} = \nabla \times (\mathbf{U} \times \mathbf{B}) + \eta \nabla^2 \mathbf{B}, \quad (2.1)$$

where  $\mathbf{U}$  is the velocity field,  $\mathbf{B}$  is the magnetic field and  $\eta$  represents the microscopic diffusivity. Dynamo theory postulates that the action of turbulence on the seed magnetic field exponentially amplifies the magnetic field countering the microscopic diffusivity. Furthermore, in a mean-field theory, it is assumed that the typical length scale of large-scale fields is  $L$  and that of the small-scale turbulent fields is  $\ell_0$ , with  $L \gg \ell_0$ . By averaging over  $\ell_0$ , and assuming that the Reynolds rules of averaging hold, we can obtain the mean-field induction equation (Steenbeck *et al.* 1966; Moffatt 1978)

$$\partial_t \langle \mathbf{B} \rangle = \nabla \times (\langle \mathbf{U} \rangle \times \langle \mathbf{B} \rangle + \mathcal{E}) + \eta \nabla^2 \langle \mathbf{B} \rangle, \quad (2.2)$$

where  $\mathcal{E} = \langle \mathbf{u} \times \mathbf{b} \rangle$  is the turbulent electromotive force (EMF), and  $\mathbf{u}$  and  $\mathbf{b}$  are the fluctuating velocity and magnetic fields, respectively.

The calculation of the turbulent EMF involves solving for the fluctuating magnetic field, which in general is a complex task. When  $Rm \ll 1$  or when the Strouhal number  $St \ll 1$ , the quasi-linear approximation (also referred to as the first-order smoothing approximation) is valid, and the fluctuating field is assumed to be generated by the action of the turbulent velocity field on the initial seed mean magnetic field. With the further assumption of homogeneity and isotropy of the turbulence (see, e.g. Brandenburg & Subramanian 2005*a*), an ansatz for the EMF can be obtained as follows:

$$\mathcal{E}_i = \alpha \langle B \rangle_i - \beta \epsilon_{ijk} \partial_j \langle B \rangle_k, \quad (2.3)$$

where  $\alpha = -\tau_u \langle \mathbf{u} \cdot \nabla \times \mathbf{u} \rangle / 3$  is related to the mean kinetic helicity  $H = \langle \mathbf{u} \cdot \nabla \times \mathbf{u} \rangle$ , and  $\beta = \tau_u \langle u^2 \rangle / 3$  is the turbulent diffusion in the kinematic regime. Here,  $\tau_u$  is the correlation time of the velocity field. At  $Rm \gg 1$  as relevant for astrophysical flows, other closure models like the eddy-damped quasi-normal Markovian approximation and the  $\tau$ -closure give similar results in the kinematic regime (Pouquet, Frisch & Leorat 1976; Blackman & Field 2002).

As turbulence is stochastic in nature, the kinetic helicity of the flow also fluctuates in time. To propose a new dynamo mechanism in non-helical turbulence (i.e. when  $\alpha$  vanishes on average), Kraichnan (1976) suggested that helicity fluctuations may have a length scale of variation,  $\ell_\alpha$ , larger than the turbulent scale  $\ell_0$ , but still smaller than the mean-field scale  $L$ . The final mean-field equation can be obtained by averaging the mean-field equation (2.2) again over the scale  $\ell_\alpha$ , i.e. a double-averaging scheme, which yields

$$\partial_t \langle \bar{\mathbf{B}} \rangle = (\beta - \alpha_{rms}^2 \tau_\alpha) \nabla^2 \langle \bar{\mathbf{B}} \rangle, \quad (2.4)$$

where  $\bar{\cdot}$  indicates the second averaging and  $\tau_\alpha$  is the correlation time of the  $\alpha$  fluctuations (in Kraichnan 1976, the terms helicity and  $\alpha$  fluctuations are used interchangeably

without distinction between them), and  $\alpha_{rms}^2 = \overline{\alpha^2}$  is the average of the square of the  $\alpha$ -fluctuations. We can define the dynamo number  $D_\alpha = \alpha_{rms}^2 \tau_\alpha / \beta$ . When  $D_\alpha > 1$ , i.e. when there is a negative diffusion in the turbulence, the double-averaged mean magnetic field grows. Thus,  $D_\alpha$  can exceed unity either when the fluctuation strength is stronger or due to the longer correlation time, and hence both these aspects are crucial for determining the dynamo action. However, in the present study, we majorly focus on the duration of the correlation time of  $\alpha$ -fluctuations as it is essential for the validity of the double-averaged mean-field equation in (2.4). In the shearing-turbulence simulation carried out by Brandenburg *et al.* (2008), the total turbulent diffusion coefficient turns out to be positive.

Several studies have investigated the role of zero-mean  $\alpha$  fluctuations and shear in explaining the dynamo observed in non-helical shear turbulence, including works by Heinemann *et al.* (2011), Mitra & Brandenburg (2012) and Jingade *et al.* (2018). In all of these models, the success of the approach depended on the existence of the temporal and spatial scale separation between the perceived fluctuations of velocity and  $\alpha$ , i.e.

$$\tau_\alpha \gg \tau_u \quad \text{and} \quad \ell_\alpha \gg \ell_0. \tag{2.5a,b}$$

In an alternate approach, Jingade & Singh (2021) utilized the renovating-flow model (Dittrich *et al.* 1984; Sokolov 1997) to directly solve for (2.1) without explicitly determining the form of the turbulent EMF. The next subsection provides a brief introduction to this approach, and also motivates the need for studying correlation times of individual Fourier modes.

### 2.2. Renovating-flow model: helicity fluctuations

In the renewing flows, time is divided into intervals  $I_n = [n\tau, (n + 1)\tau]$  of length  $\tau$  for  $n = 0, 1, 2, \dots$ . A random flow  $\mathbf{u}(t, \mathbf{x})$  is generated by choosing

$$\mathbf{u}(t, \mathbf{x}) = \mathbf{u}_\tau(t - n\tau, \mathbf{x}), \tag{2.6}$$

for each interval  $I_n$ , where  $\mathbf{u}_\tau$  is chosen randomly from the ensemble  $\Sigma_\tau$  of smooth flows, given by

$$\Sigma_\tau = \{\mathbf{u}_\tau(t, \mathbf{x}) : 0 \leq t < \tau\}. \tag{2.7}$$

The velocity fields in each interval are considered to be random and statistically independent realizations of the underlying probability distribution function. The random velocity field of the ensemble  $\Sigma_\tau$  is chosen to be a single-scale finite time solution of the Navier–Stokes equation without the Lorentz force (see Jingade & Singh 2021 for details). The model velocity field  $\mathbf{u}(t, \mathbf{x}; S, \mathbf{q}, h)$  hence depends on a number of parameters:  $S$  is a constant shear rate so that the background shear flow is of the form  $\mathbf{U}^{shear} = Sx\mathbf{e}_y$ ,  $\mathbf{q} = (q_1, q_2, q_3)$  is the wave vector of  $\mathbf{u}_\tau$  at initial time and the value of  $h$  controls the relative helicity of the flow  $\mathbf{u}$  which varies in the range  $[-1, 1]$ .

Under the assumption of statistical independence of the velocity field across the intervals, the evolution of the magnetic field equation can be written separately for any given interval  $[(n - 1)\tau, n\tau]$  in Fourier space. Specifically, the magnetic field at time  $n\tau$  can be written in terms of the initial magnetic field at time  $(n - 1)\tau$ , after averaging over the initial randomness of the magnetic field and the statistical ensemble of the velocity

field, as (see Jingade & Singh 2020 for details)

$$\mathbf{B}(n\tau, \mathbf{k}) = \mathbf{G}(\tau, \mathbf{k})\mathbf{B}_0((n-1)\tau, \mathbf{k}), \quad (2.8)$$

where  $\mathbf{G}$  is a response tensor that describes the average deformation of fluid particle trajectories over the interval  $\tau$  due to the velocity field statistics. The response tensor is obtained by neglecting the diffusion term in the induction equation. As a result, the magnetic field at specific realizations exhibits fine structures similar to those at large  $Rm$ . However, the averaging over the velocity statistics introduces the effective turbulent diffusivity for the growing magnetic field, smoothing the field over the turbulent velocity scale.

In the renovating-flow model presented by Jingade & Singh (2021), the idea of helicity fluctuations introduced by Kraichnan (1976) and Sokolov (1997) is incorporated. In this model, the helicity of the flow is assumed to take independent and random values in successive time intervals, while the durations of these intervals are fixed. It is also assumed that the renovation time of helicity,  $\tau_h$ , is an integral multiple of the renovation time of the velocity field,  $\tau$ , i.e.  $\tau_h = m\tau$ , where  $m \geq 2$  and  $\tau$  is the correlation time of the flow. In (2.8), the response tensor is averaged over the statistics of the velocity field, except for the helicity parameter  $h$ . To incorporate the helicity fluctuation and its time-scale separation in the averaging, the response tensors from adjacent intervals are multiplied together while the helicity is fixed over the  $m$  intervals. Later, the product of the response tensor is averaged over the helicity statistics to obtain the double-averaged mean field. Thus, the magnetic field at time  $n\tau$  can be expressed in terms of the magnetic field at  $(n-m)\tau$  as

$$\mathbf{B}(n\tau, \mathbf{k}) = \mathcal{G}(\tau, \mathbf{k})\mathbf{B}_0((n-m)\tau, \mathbf{k}), \quad (2.9)$$

$$\mathcal{G}(\tau, \mathbf{k}) = \langle \mathbf{G}(\tau, \mathbf{k}_{n-1}) \dots \mathbf{G}(\tau, \mathbf{k}_{n-m}) \rangle_h, \quad (2.10)$$

where  $\mathcal{G}(\tau, \mathbf{k})$  is the double-averaged response tensor, whose eigenvalues determine the growth rate and cycle period of the dynamo wave (see Jingade & Singh 2021 for details). It is shown that a non-helical large-scale dynamo can be generated only when the ratio between the time scales is  $\geq 3$ .

### 2.3. Sources of helicity fluctuations

In non-helical turbulence, the kinetic helicity fluctuates around zero, and these fluctuations have two primary contributions. The first contribution arises from the non-equivalence of volume averaging and ensemble averaging. In renovating flows, averaging is conducted over the ensemble of the velocity field, strictly adhering to the Reynolds-averaging rule. Conversely, in mean-field theory, averaging is performed over a length scale or a finite volume, leading to an approximate adherence to Reynolds' rules, as argued by Hoyng (1987, 1988) and Zhou, Blackman & Chamandy (2018). In the work by Hoyng, the resulting error terms manifest as a forcing term in the mean-field equation, giving rise to fluctuations in the transport coefficients, whereas in the work by Zhou *et al.* (2018), the deviation from Reynolds' rules introduces additional terms in the mean-field equations, but these appear as spatial gradients of the mean fields. Since volume average is not strictly equivalent to an ensemble average, the volume-averaged mean helicity  $H$  fluctuates over time in simulations of non-helical turbulence, although typically with relatively small amplitudes (see figure 1 in the supplementary material available at <https://doi.org/10.1017/jfm.2024.1006> for the evolution of the volume-averaged helicity). We denote the correlation time of  $H$  as  $\tau_H$ , which serves as our first analogue to the correlation time of  $\alpha$  fluctuations.



Note that the volume-averaged helicity scales as  $V^{-1/2}$ , where  $V$  is the volume of the box, assuming the helicity fluctuations within each eddy remain consistent regardless of the volume. Furthermore, if the helicity fluctuations in each eddy are independent and identically distributed with a uniform correlation time  $\tau_0$ , then the correlation time of the mean helicity will also be  $\tau_0$ , independent of the volume. In this study, we examine how the correlation time varies with rotation or shear rate, keeping the volume fixed. The implications of finite volume, such as a scale-dependent dynamo growth rate, could be significant for astrophysical dynamos and will be explored in future work.

The second contribution to helicity fluctuations arises from the intrinsic randomness of turbulence, where the helicity associated with each Fourier mode fluctuates around zero due to the nonlinear interaction of waves. Consequently, our second analogue to the correlation time of helicity fluctuations pertains to individual flow modes rather than volume-averaged quantities. Compared with  $\tau_H$ , this idea aligns more closely with the renovating-flow model by Jingade & Singh (2021), where a single-scale flow is used to investigate the dynamo phenomenon, associating fluctuating helicity at a particular mode  $\mathbf{q}$  with some correlation time.

However, real turbulence involves multiple scales. The single-scale model of Jingade & Singh (2021) can be extended to multi-scale flows by constructing the velocity field from independent non-interacting helical waves, with amplitudes following specific power laws across scales (see Singh & Sridhar 2017 for details). In turbulence's steady state, the nonlinear term only cascades energy across scales, leaving the dynamics of individual modes unaffected. This extension justifies our scale-by-scale approach to verifying the dynamo action criteria. Similar methods have been employed by Wilkin, Barenghi & Shukurov (2007) and others to study dynamo problems. Consequently, our objective is to determine the correlation times of both velocity and helicity fields across a spectrum of wave vectors  $\mathbf{k}$  and verify the dynamo criteria scale by scale.

The correlation time of the helicity field is obtained by considering the helicity density in Fourier space, defined as

$$\tilde{g}(t, \mathbf{k}) = \tilde{\mathbf{u}}^*(t, \mathbf{k}) \cdot \mathbf{i}\mathbf{k} \times \tilde{\mathbf{u}}(t, \mathbf{k}), \quad (2.11)$$

where  $\tilde{\mathbf{u}}$  is the Fourier transform of the velocity field. It is important to note that  $\tilde{g}$  is a real quantity and represents the helicity of the velocity field of a particular mode  $\mathbf{k}$  and at time  $t$ . We must distinguish  $\tilde{g}$  from the Fourier transform of the helicity density in configuration space,  $h = \mathbf{u} \cdot \nabla \times \mathbf{u}$ , which is not used in our analysis.

### 3. General definitions and numerical methods

#### 3.1. Velocity and helicity auto-correlations

In theoretical analysis, ensemble averages are often used to define averages of a quantity in turbulence. However, in simulations, ensembles are often not available, and the turbulent field at different times can be treated as copies of the ensemble, provided the turbulence is stationary. In our simulations, we perform the statistical averaging of the velocity field over time. The equivalence between the ensemble average discussed in the previous section and the temporal average is ensured by the ergodic theorem. The correlation times of velocity and helicity fluctuations are computed through their auto-correlation functions. We define the auto-correlation function of a velocity field  $\mathbf{u}(t, \mathbf{x})$  at the space point location  $\mathbf{x}$  as

$$\mathcal{T}_u(\tau, \mathbf{x}) \equiv \int_{t_0}^{\infty} dt [\mathbf{u}(t + \tau, \mathbf{x}) - \bar{\mathbf{u}}(\mathbf{x})] \cdot [\mathbf{u}(t, \mathbf{x}) - \bar{\mathbf{u}}(\mathbf{x})], \quad (3.1)$$

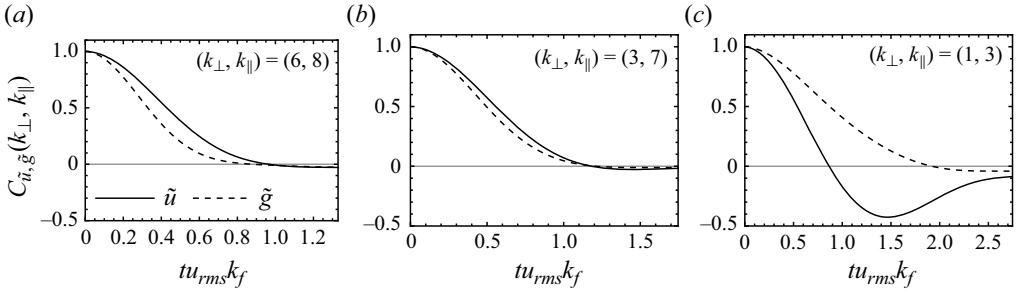


Figure 1. Three typical auto-correlation curves for run R3, demonstrating how the correlation times of the velocity and helicity fluctuations vary with the wavenumbers parallel ( $k_{\parallel}$ ) and perpendicular ( $k_{\perp}$ ) to the rotation axis.

where  $t_0$  represents the initial time of the simulations when turbulence has become stationary and an overbar denotes a time average. Similarly, the auto-correlation of the Fourier transform of the velocity is defined as

$$\mathcal{T}_{\tilde{u}}(\tau, \mathbf{k}) \equiv \int_{t_0}^{\infty} dt [\tilde{\mathbf{u}}(t + \tau, \mathbf{k}) - \bar{\tilde{\mathbf{u}}}(\mathbf{k})] \cdot [\tilde{\mathbf{u}}(t, \mathbf{k}) - \bar{\tilde{\mathbf{u}}}(\mathbf{k})]^*, \quad (3.2)$$

where the asterisk indicates the complex conjugate.

We also define the auto-correlations of the mean helicity as

$$\mathcal{T}_H(\tau) = \int_{t_0}^{\infty} dt [H(t + \tau) - \bar{H}] \cdot [H(t) - \bar{H}], \quad (3.3)$$

where  $H(t) = \int d^3x \mathbf{u}(t, \mathbf{x}) \cdot \boldsymbol{\omega}(t, \mathbf{x}) = \int d^3k \tilde{g}(t, \mathbf{k})$ , and  $\boldsymbol{\omega} = \nabla \times \mathbf{u}$  is the vorticity field. Here,  $H$  has a vanishing ensemble-average mean, but in simulations they fluctuate around zero, as discussed in § 2.3. The auto-correlation of the helicity density  $\tilde{g}(\mathbf{k}, t)$  in the Fourier space is

$$\mathcal{T}_{\tilde{g}}(\tau, \mathbf{k}) \equiv \int_{t_0}^{\infty} dt [\tilde{g}(t + \tau, \mathbf{k}) - \bar{\tilde{g}}(\mathbf{k})] \cdot [\tilde{g}(t, \mathbf{k}) - \bar{\tilde{g}}(\mathbf{k})]^*. \quad (3.4)$$

Finally, we define the volume-integrated correlation function as

$$C_u(t) = \int d^3x \mathcal{T}_u(t, \mathbf{x}) = \int \frac{d^3k}{(2\pi)^3} \mathcal{T}_{\tilde{u}}(t, \mathbf{k}). \quad (3.5)$$

The second equality is due to Parseval's theorem.

Figure 1 displays three typical auto-correlation curves of run R3 (further details can be found in § 4). The correlation time of an auto-correlation curve is determined by fitting its initial positive part with an exponentially decaying curve and identifying the time at which its value reaches  $1/e$  of its maximum. We denote the correlation time of  $\mathcal{T}_I$  by  $\tau_I$ , where  $I \in \{u, \tilde{u}, g, \tilde{g}, H\}$ .

### 3.2. Distinguishing different helicity time scales

A volume-integrated correlation function for the helicity modes is defined by integrating the helicity auto-correlation function over the wave vector space, similar to (3.5)

$$C_g(t) = C_{\tilde{g}}(t) = \int \frac{d^3k}{(2\pi)^3} \mathcal{T}_{\tilde{g}}(t, \mathbf{k}). \quad (3.6)$$



### Correlation time of velocity and kinetic helicity

It should be noted that, although one might expect the correlation times of  $C_g$  and  $C_H$  to be similar, this is not necessarily the case. To see the reason, we assume that  $\tilde{g}(\mathbf{k})$  has a vanishing mean for the moment and note that

$$C_H = \int dt' \int \frac{d^3k_1}{(2\pi)^3} \tilde{g}(t', \mathbf{k}_1) \int \frac{d^3k_2}{(2\pi)^3} \tilde{g}(t' + t, \mathbf{k}_2), \quad (3.7)$$

$$C_g = \int \frac{d^3k}{(2\pi)^3} \int dt' \tilde{g}(t', \mathbf{k}) \tilde{g}(t' + t, \mathbf{k}). \quad (3.8)$$

It is clear from (3.7) and (3.8) that  $C_H$  is the auto-correlation of the sum of all modes, whereas  $C_g$  is proportional to the mean of the auto-correlations over all modes.

Both  $\tau_g$  and  $\tau_H$  have been utilized in dynamo models, each with its own significance. In the original negative diffusion model proposed by Kraichnan (1976), the time scale for fluctuations of the  $\alpha$  coefficient was closely related to  $\tau_H$ . Similarly, stochastic  $\alpha$  dynamo models, such as those by Vishniac & Brandenburg (1997) and Richardson & Proctor (2012), also adopt a time scale associated with  $\tau_H$ . On the other hand, researchers studying turbulence using random waves, as exemplified by Jingade & Singh (2021), focus on the damping time of a single helical wave and therefore utilize  $\tau_g$ . In our study, we present results for both  $\tau_g$  and  $\tau_H$ , recognizing the importance of considering both perspectives.

### 3.3. Numerical set-ups and methods

Focusing on the kinematic dynamo regime and neglecting Lorentz forces, we perform compressible isothermal hydrodynamic simulations of isotropically and non-helicity forced turbulence using the publicly available PENCIL CODE (Pencil Code Collaboration *et al.* 2021). The equations to be solved are

$$D_t \ln \rho = -\nabla \cdot \mathbf{u}, \quad (3.9)$$

$$D_t \mathbf{u} = S u_x \mathbf{e}_y - c_s^2 \nabla \ln \rho - 2\boldsymbol{\Omega} \times \mathbf{u} + \frac{1}{\rho} \nabla \cdot (2\rho \nu \mathbf{S}) + \mathbf{f}, \quad (3.10)$$

where  $D_t = \partial_t + \mathbf{u} \cdot \nabla + Sx\partial_y$ ,  $S$  is the shear rate of the shear flow  $U^{shear} = Sx\mathbf{e}_y$ ,  $c_s$  is a constant sound speed,  $\nu$  is the viscosity and  $\mathbf{S}_{ij} = (\partial_i u_j + \partial_j u_i)/2 - \delta_{ij} \nabla \cdot \mathbf{u}/3$  is the rate-of-strain tensor. In the burgulence cases, the density equation (3.9) is dropped and the second term on the right-hand side of (3.10) is set identically to zero, turning the Navier–Stokes equations into Burgers' equation. The rotation rate  $\boldsymbol{\Omega} = \Omega \mathbf{e}_z$  is applied along the  $z$ -direction, and the random force  $\mathbf{f}$  takes the form of a non-helical plane wave (see Brandenburg 2001 for details). The forcing wave vector has a fixed magnitude  $k_f$ , but its phases and directions change at each time step. The simulation box has dimensions  $L^3 = (2\pi)^3$  with periodic boundary conditions in all the directions or shear-periodic (in the case of shear) boundary conditions in the  $x$ -direction. In all runs, the forcing wavenumber is  $k_f = 5$ , and the Mach number is approximately 0.1. A summary of the runs is provided in table 1, which includes the Reynolds number  $Re = u_{rms}/(\nu k_f)$ , the Coriolis number  $Co = 2\Omega/(u_{rms} k_f)$  and the dimensionless shear number  $Sh = -S/(u_{rms} k_f)$ . For the rotating turbulence cases R1 to R5, we compute the Coriolis number by excluding the  $k < k_f$  modes when computing the root-mean-square velocity  $u_{rms}$  (see § 4). We denote the Coriolis number computed using this definition of  $u_{rms}$  as  $Co_f$ . For runs R3 to R5, their Coriolis numbers are sufficiently large to allow for condensation of large-scale vortices, and therefore their Reynolds numbers are apparently higher than those of runs R1 to R2.

Run	$N^3$	$Ma$	$q = -S/\Omega$	$Re$	$Co$ or $Co_f$	$Sh$	$k_{ze}$
NH	$256^3$	0.12	/	45.93	0	0	/
R1	$256^3$	0.02	0	32.17	0.43	0	0.35
R2	$256^3$	0.03	0	33.14	0.86	0	5.19
R3	$256^3$	0.07	0	90.34	2.03	0	14.24
R4	$256^3$	0.08	0	108.06	3.20	0	25.68
R5	$256^3$	0.09	0	115.94	4.29	0	40.75
S1	$256^3$	0.12	-4	46.86	0.03	0.07	/
S2	$256^3$	0.14	-4	55.34	0.11	0.22	/
S3	$256^3$	0.16	-4	64.62	0.29	0.57	/
S4	$256^3$	0.13	-4	50.47	0.76	1.52	/
S5	$256^3$	0.11	-8	42.15	0.91	3.65	/
SB1	$256^3$	/	-4	15.10	0.04	0.08	/
SB2	$256^3$	/	-4	15.31	0.15	0.31	/
SB3	$256^3$	/	-4	14.21	0.50	1.00	/
SB4	$256^3$	/	-4	11.95	1.24	2.48	/
K1	$256^3$	0.12	3/2	47.62	0.13	0.10	/
K2	$256^3$	0.13	3/2	49.80	0.74	0.56	/
K3	$256^3$	0.12	3/2	45.60	1.69	1.27	/
K4	$256^3$	0.11	3/2	41.96	3.67	2.75	/
K5	$256^3$	0.10	3/2	37.36	8.24	6.18	/

Table 1. A summary of runs, where  $N^3$  is the resolution,  $Ma = u_{rms}/c_S$  is the Mach number,  $S$  is the shear rate,  $\Omega$  is the rotation rate,  $Re = u_{rms}/\nu k_f$  is the Reynolds number,  $Co = 2\Omega/u_{rms}k_f$  is the Coriolis number,  $Sh = -S/u_{rms}k_f$  is the dimensionless shear rate and  $k_{ze}$  is the Zeman wavenumber. For rotation runs R1 to R5, the root-mean-squared velocity used for computing the Coriolis number excludes large-scale modes with  $k < k_f$ , and therefore their Coriolis numbers will be denoted by  $Co_f$  rather than  $Co$ . For these runs the Zeman wavenumber  $k_{ze}$  is also listed. The runs SB1 to SB4 solve the Burgers' equation and the Mach number is undefined.

At even higher values of  $Co_f$ , the flow becomes quasi two-dimensional and dynamos will not be supported (Cowling 1933). Therefore, we exclude the exploration of high Coriolis numbers.

In this study, particular attention is given to ensuring the hydrodynamic stability of the flow in all simulations. The choice of shear rate and rotation rate is made such that the flow remains stable throughout the simulations. This criterion for stability,  $-\infty < -S/\Omega < 2$ , as discussed in Salhi (2002) and Balbus & Hawley (2006), has been taken into consideration. The presence of instabilities in the flow could lead to vorticity dynamos (Käpylä, Mitra & Brandenburg 2009), i.e. the generation of additional mean flows. Such mean flows would render the system non-ergodic. To ensure the validity of measurements that require time stationarity such as the temporal average of the correlation functions, it is essential to prevent such instabilities from affecting the measurements.

We use two methods to generate auto-correlation curves of the velocity and helicity fluctuations. In the first method, we output the time series data for  $\tilde{\mathbf{u}}(t, \mathbf{k})$  from the simulations and calculate auto-correlation curves during post-processing. The duration of time series for all runs spans at least 200 times the eddy turnover time  $1/(u_{rms}k_f)$  with a sampling frequency of no less than  $10u_{rms}k_f$ . For runs with the highest shear rates (S4, S5, SB4, K4 and K5), the sampling frequency is increased to a minimum of  $20u_{rms}k_f$ .

## Correlation time of velocity and kinetic helicity

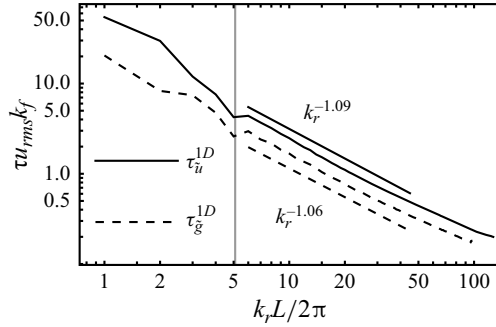


Figure 2. For run NH, correlation times of shell-averaged auto-correlations for velocity (solid) and helicity (dashed) fields. The vertical line indicates the forcing wavenumber at  $k_f = 5$ .

This approach allows for obtaining auto-correlations for individual Fourier modes. As large-scale flow patterns such as shear or rotation primarily influence the larger scales of the flow, we have limited the output to the range  $-2k_f \leq k_{x,y,z} \leq 2k_f$ , which has been confirmed to encompass the energy-dominant modes.

The first method needs high data output frequency and therefore is only applied to a limited range of wave modes. In the second method, correlation functions are computed on the fly and for all the wave modes, although this approach results in a smaller sample size for time averaging. The method is specifically used to obtain shell-averaged correlation functions in the Fourier space. To implement this, we regularly update a time-independent auxiliary field  $\tilde{\mathbf{v}}(\mathbf{k})$  to match  $\tilde{\mathbf{u}}(t, \mathbf{k})$  at specific time intervals (every  $\Delta t = 50$  in code units, roughly 27 times the eddy turnover time of the isotropic run). The field  $\tilde{\mathbf{v}}(\mathbf{k})$  is kept fixed between updates. At a given update time  $t_0$ , we set  $\tilde{\mathbf{v}}_0(\mathbf{k})$  to be the value of  $\tilde{\mathbf{u}}(t_0, \mathbf{k})$ . During the interval  $t_0 \leq t < t_0 + \Delta t$ , the velocity auto-correlation between  $\tilde{\mathbf{v}}_0(\mathbf{k})$  and  $\tilde{\mathbf{u}}(t, \mathbf{k})$  is computed as

$$\mathcal{T}_{\tilde{u}}(t, \mathbf{k}) = \tilde{\mathbf{v}}_0^*(\mathbf{k}) \cdot \tilde{\mathbf{u}}(t_0 + t, \mathbf{k}) = \tilde{\mathbf{u}}^*(t_0, \mathbf{k}) \cdot \tilde{\mathbf{u}}(t_0 + t, \mathbf{k}), \quad 0 \leq t \leq \Delta t. \quad (3.11)$$

Similarly, the helicity correlation  $\mathcal{T}_{\tilde{g}}$  is computed. These correlation curves are then averaged at discrete intervals.

While this method allows us to analyse modes at the largest wavenumbers, it limits the number of averaged ensemble members to  $T/\Delta t$ , where  $T$  is the overall time duration of the simulation.

In [figure 2](#), we present correlation times for shell-averaged quantities in isotropic non-helical turbulence. The shell-averaged correlation functions are defined by

$$C_{\tilde{u}, \tilde{g}}(t, k_r) = \frac{1}{4\pi} \int \sin \theta \, d\theta \, d\phi \mathcal{T}_{\tilde{u}, \tilde{g}}(t, \mathbf{k}), \quad (3.12)$$

where  $(k_r, \theta, \phi)$  are the spherical coordinates in Fourier space. Subsequently, the correlation times for each wavenumber are fitted as  $\tau_u^{1D}(k_r)$  and  $\tau_g^{1D}(k_r)$  for the velocity and helicity auto-correlations, respectively. The identified  $k_r^{-1}$  power law for  $\tau_u^{1D}$  in [figure 2](#) suggests that the Eulerian correlation time is primarily influenced by the sweeping effect, where small-scale eddies are transported by larger-scale eddies. Consequently,  $\tau_u^{1D} \propto 1/(u_{rms} k_r)$ , aligning with findings from prior theoretical and numerical studies (Chen & Kraichnan 1989; Sanada & Shanmugasundaram 1992; Favier, Godefert & Cambon 2010; Clark Di Leoni, Cobelli & Mininni 2015).

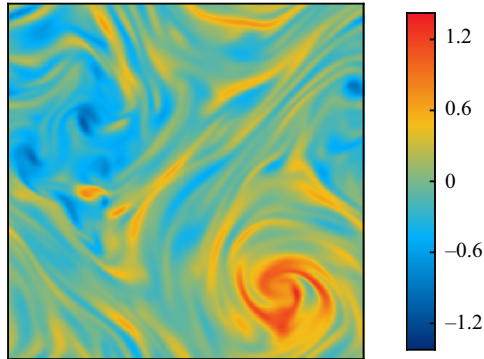


Figure 3. The  $z$  component of the vorticity field (normalized by  $k_f u_{rms}$ ) at the  $z = 0$  slice for run R4 in the steady state.

We have also computed the correlation time of the volume-integrated velocity or helicity correlation, along with that of the total helicity using (3.3), (3.5) and (3.6). The obtained values are

$$\tau_u u_{rms} k_f = 3.11, \quad \tau_H / \tau_u = 2.42, \quad \tau_g / \tau_u = 0.61. \quad (3.13a-c)$$

These values serve as a set of fiducial references, which we will compare with the results obtained when rotation or shear is introduced. Brandenburg & Subramanian (2005b) previously reported a Strouhal number  $St = \tau_u u_{rms} k_f$  around unity for the  $\mathbf{u} \cdot \boldsymbol{\omega}$  correlation, determined by dividing the  $\alpha$  coefficient from a test-field method by one third of the mean kinetic helicity. Our value of 3.11 is not fundamentally at odds with this, mainly due to the different methods and, consequently, the different definitions of  $\tau_u$  employed.

In the next two sections, we present the measured correlation times for velocity and helicity fluctuations in rotating and shearing turbulence, respectively. A more detailed discussion of the implications for the shear dynamo problem along with the comparison with previous simulation results is provided in § 6.

#### 4. Rotating flows

In this section, we compare the correlation times of velocity and helicity fluctuations in rotating turbulence. Rotating turbulence is known to form a condensate through the inverse cascade of energy and, in a steady state, counter-rotating vortices are formed to cancel the effect of global rotation (this is a consequence of the generalization of the Kelvin vorticity theorem in a rotating frame and it is known as Bjerkne’s theorem) (Kraichnan 1967; Bartello, Metais & Lesieur 1994; Alexakis 2015). The rotation tends to suppress velocity gradients along the direction of rotation, making the flow quasi-two-dimensional at sufficiently large Coriolis numbers.

In figure 3, the  $z$  component of the vorticity field at the  $z = 0$  slice for run R4 is plotted at the steady-state regime of the simulation, and we observe asymmetric cyclonic and anti-cyclonic vortices aligned in the direction of rotation (also seen in Seshasayanan & Alexakis (2018), Dallas & Tobias (2018) and the references therein). The vortices display an asymmetry in their positive and negative strengths, with cyclonic vortices having a comparatively higher strength than anti-cyclonic vortices. This is because one of the vortices is Rayleigh stable for a given sign of rotation and strength (Tritton & Davies 1985). The formation of these vortices will alter the estimate of the correlation time of both velocity and helicity fluctuations.

## Correlation time of velocity and kinetic helicity

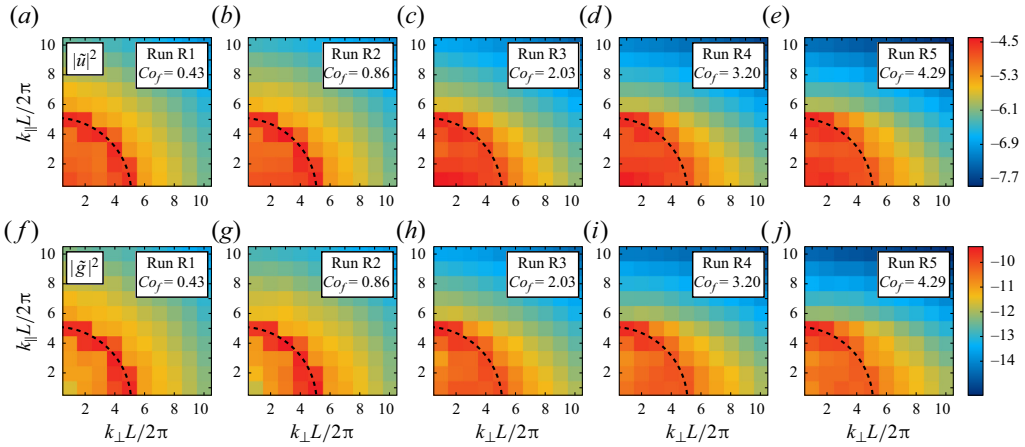


Figure 4. For rotating turbulence, the velocity ( $|\tilde{u}|^2$ ,  $a$ – $e$ ) and helicity ( $|\tilde{g}|^2$ ,  $f$ – $j$ ) energy densities on a  $\log_{10}$  scale. The dashed curves indicate the forcing wavenumber  $k_f = 5$ .

Since our interest is in the large-scale dynamics, we focus on the turbulent flow and therefore exclude the  $k < k_f$  modes when computing the root-mean-square velocity  $u_{rms}$ . We denote the Coriolis number computed using this definition of  $u_{rms}$  as  $Co_f$ . At sufficiently large wavenumbers where the isotropic eddy turnover rate is larger than the rotation rate, the turbulence is expected to recover the Kolmogorov scaling with a power-law energy distribution of  $k^{-5/3}$ . The scale at which this transition occurs is referred to as the Zeman scale, given by  $k_{ze} = (\Omega^3/\epsilon)^{1/2}$ , where  $\epsilon = (\mathbf{u} \cdot \mathbf{f})$  is the energy injection rate. This is the scale at which the rotation rate  $\Omega$  equals the eddy turnover rate  $k\tilde{u}(k)$  (Zeman 1994).

The properties of the flow are different in the direction of rotation ( $\hat{k}_{||}$ ) and in the direction perpendicular to it ( $\hat{k}_{\perp}$ ), presenting axial symmetry. We therefore obtain the correlation functions by performing the azimuthal average as

$$C_{\tilde{u},\tilde{g}}^{axi}(t, k_{\perp}, k_{||}) = \frac{1}{2\pi} \int d\phi \mathcal{T}_{\tilde{u},\tilde{g}}(t, \mathbf{k}). \quad (4.1)$$

Additionally, we average over modes with the same  $|k_{||}|$ , because the correlation functions of velocity or helicity are invariant under coordinate reflection over the  $k_{||} = 0$  plane.

Note that  $C_{\tilde{u},\tilde{g}}^{axi}(t = 0, k_{\perp}, k_{||})$  are just the velocity and helicity energy densities (i.e. quadratic in  $\tilde{u}$  or  $\tilde{g}$ ), which we show in figure 4. For the nearly isotropic cases R1 and R2, both velocity and helicity energy densities concentrate near the forcing scale  $k_f = 5$ . At high rotation rates, the velocity energy density smears into the low- $k$  region manifesting the large-scale vortices, and the helicity modes favour to reside along the  $k_{||}$  direction.

The correlation times, denoted as  $\tau_{\tilde{u}}^{axi}(k_{\perp}, k_{||})$  and  $\tau_{\tilde{g}}^{axi}(k_{\perp}, k_{||})$  for velocity and helicity fluctuations, respectively, are estimated by fitting the positive part of the correlation function to an exponential curve, as described in § 3.1. Figure 1 displays three representative auto-correlation curves for run R3, which show that helicity fluctuations become increasingly coherent over time as we move to smaller-wavenumber regions in the Fourier space. This coherence is a result of the formation of cyclonic and anti-cyclonic vortices in the rotating turbulence. Visualizing this phenomenon of increasing correlation time of helicity, fluid elements entering these vortices would follow a spiralling trajectory, and the helicity sign of these elements would be contingent upon the angle of entrance relative to the vortices' axis.

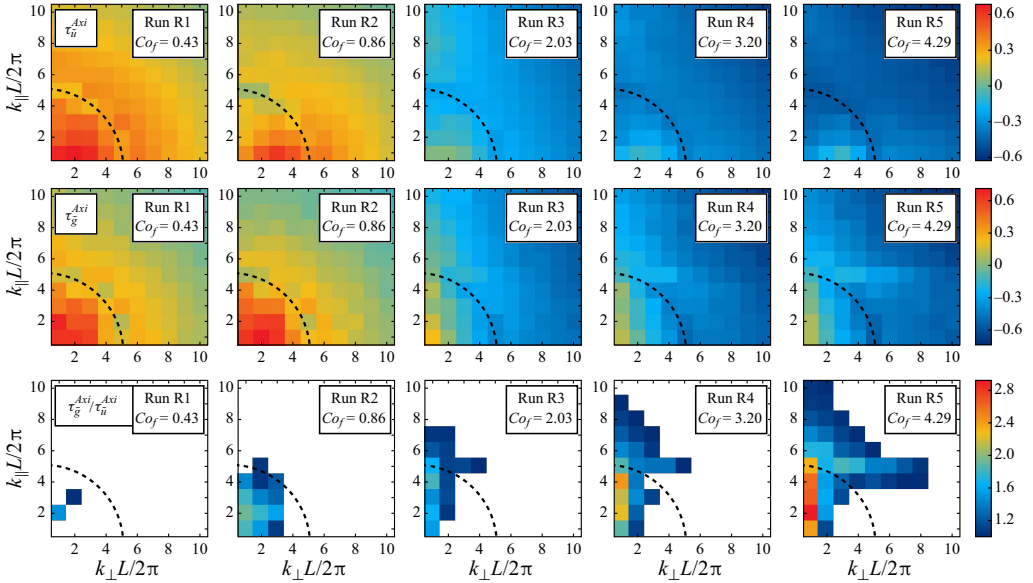


Figure 5. For rotating turbulence, the first and second rows show the correlation times of velocity and helicity fluctuations in the  $k_{\perp} - k_{\parallel}$  plane, respectively. The correlation times are normalized by the eddy turnover time  $1/(k_f u_{rms})$  and displayed on a  $\log_{10}$  scale. Here,  $u_{rms}$  excludes large-scale modes with wavenumbers  $k < k_f$  and  $k_f$  denotes the forcing scale, indicated by the black dashed curve at  $k_f = 5$ . The third row shows the ratio of these two times on a linear scale, which is displayed only for the region where the ratio is equal to or greater than unity.

The correlation times for a range of  $(k_{\perp}, k_{\parallel})$  pairs are displayed in the first two rows of figure 5. In the third row of the same figure, the ratio of the helicity to velocity coherence times,  $\zeta^{axi} \equiv \tau_g^{axi} / \tau_u^{axi}$ , is displayed for regions where  $\zeta^{axi} \geq 1$ , highlighting the modes for which the coherence time of helicity fluctuations is longer than that of velocity fluctuations, therefore potentially capable of driving large-scale dynamos (Jingade & Singh 2021). This should be contrasted with figure 2 and (3.13), where the opposite trend  $\zeta < 1$  is seen for all the wavenumbers in the isotropic case. With increasing rotation rate, an increase in both the area where  $\zeta^{axi} \geq 1$  and the maximum values of  $\zeta^{axi}$  can be observed. The Zeman scale, which is the scale at which the rotation rate becomes equal to the eddy turnover time, has also been computed for all the runs and is provided in table 1. As seen from the table, the scales where  $\zeta^{axi} = \tau_g^{axi} / \tau_u^{axi} > 1$  are within the Zeman scale for runs R1 and R2, indicating that the difference in coherence times is a result of the rotation rate having a significant impact at these scales. For runs R3 to R5, the Zeman wavenumbers are out of the plotted range. Nevertheless, the condition  $\zeta^{axi} > 1$  predominantly occurs within the region  $k < k_{ze}$ .

For volume-averaged time scales, in order to exclude the impact from the secondary mean flows generated by large-scale vortices, we calculated the volume-integrated auto-correlation for the small-scale fields by summing over all the Fourier modes with  $k \geq k_f$

$$C_u(t) = \int_{|k| \geq k_f} \frac{d^3 k}{(2\pi)^3} \mathcal{T}_{\bar{u}}(t, \mathbf{k}), \quad (4.2)$$



### Correlation time of velocity and kinetic helicity

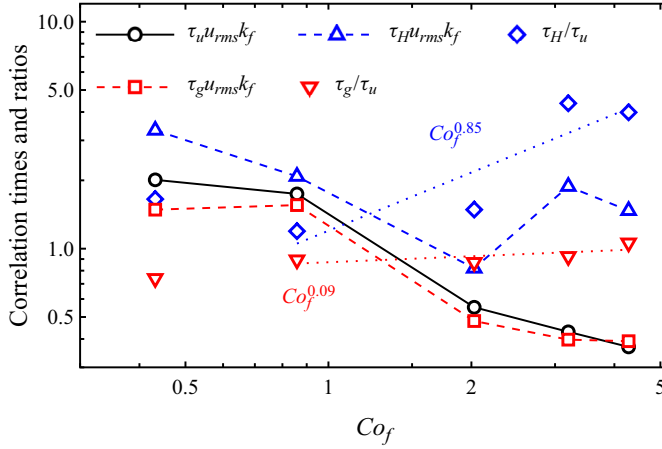


Figure 6. For weakly compressible rotating turbulence, the volume-averaged velocity and helicity correlation times, and their ratios. Here,  $Co_f$  is the Coriolis number  $2\Omega/(u_{rms}k_f)$ , with  $u_{rms}$  excluding the modes with  $k < k_f$ . The dotted blue and dashed red lines are the fitted power-law relations for  $\tau_H/\tau_u$  and  $\tau_g/\tau_u$ , respectively.

$$C_H(\tau) = \int_{t_0}^{\infty} dt [H_f(t + \tau) - \overline{H_f}] \cdot [H_f(t) - \overline{H_f}], \quad \text{with } H_f = \int_{|\mathbf{k}| \geq k_f} \frac{d^3k}{(2\pi)^3} \tilde{g}(\mathbf{k}), \quad (4.3)$$

$$C_g(t) = \int_{|\mathbf{k}| \geq k_f} \frac{d^3k}{(2\pi)^3} \mathcal{T}_{\tilde{g}}(t, \mathbf{k}). \quad (4.4)$$

This analysis includes all the small-scale modes and is complementary to figure 5, which only considered wavenumbers up to  $2k_f$ . In figure 6, we present the correlation times obtained from these correlators. As the Coriolis number  $Co_f$  increases, all the three dimensionless times scales  $\tau_{u,g,H}u_{rms}k_f$  decrease, with  $\tau_H u_{rms}k_f$  decreasing at a slightly lower rate. Meanwhile, the ratios of the time scales  $\tau_{H,g}/\tau_u$  increase with increasing  $Co_f$ , although with a rather weak dependence, as indicated by the dotted lines in the figure. The ratio  $\tau_g/\tau_u$  never exceeds unity even at the largest rotation rate we have explored, whereas the ratio  $\tau_H/\tau_u$  has a larger magnitude and is always above unity. The trend of the ratio  $\tau_g/\tau_u$  for the modes  $k > k_f$  appears to be unaffected by the rotation rate, suggesting that these modes are unimportant for large-scale dynamo action.

In addition to the helicity correlation time, the efficiency of the incoherent  $\alpha$  effect also depends on the amplitude of helicity fluctuations (see (2.4)). In figure 7, we depict the probability density functions (PDFs) of the relative helicity,  $\tilde{g}/k|\tilde{u}|^2$ , for 10 different representative modes with varying scales, across all runs. The relative helicity is defined such that, when the mode at wavenumber  $\mathbf{k}$  is fully helical,  $\tilde{g}/k|\tilde{u}|^2 = \pm 1$  (corresponding to positively or negatively helical cases), and it becomes 0 when the mode is non-helical. Partially helical modes have relative helicities between  $\pm 1$ . The PDFs for the low-wavenumber modes ( $k < k_f$ ) tend to have a non-zero mean, indicative of the presence of asymmetric counter-rotating large-scale vortices that affect the distribution of helicity fluctuations. On the other hand, the PDFs for the high-wavenumber modes ( $k > k_f$ ) exhibit symmetry around zero and are nearly uniform in nature.

We can estimate the dynamo number, which is the ratio of the strength of the helicity fluctuations to the turbulent diffusivity (see the discussion below (2.4)), by utilizing

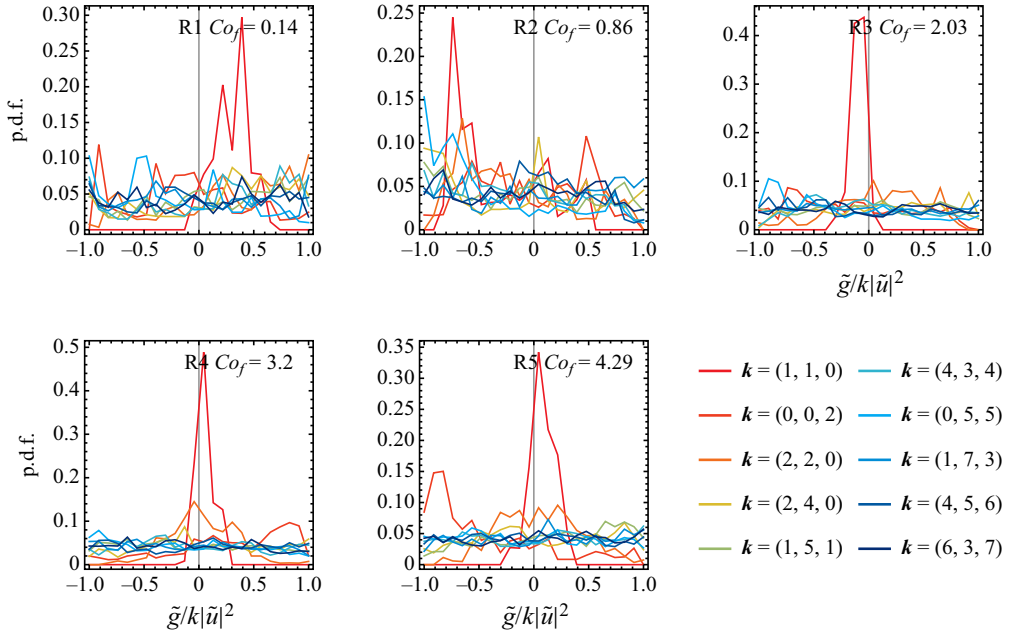


Figure 7. Probability density functions of the normalized helicity  $\tilde{g}/k|\tilde{u}|^2$  for a few modes for the rotating turbulence runs.

$\alpha_{rms} \simeq \tau_u H_{rms}/3$  (with  $H_{rms}$  being the root-mean-square value of the fluctuating mean kinetic helicity  $H$ ),  $\beta \simeq \tau_u u_{rms}^2/3$  and either  $\tau_\alpha = \tau_H$  or  $\tau_g$  as follows:

$$D_{H,g} \simeq \frac{\tau_{H,g} \alpha_{rms}^2}{\tau_u u_{rms}^2/3} \simeq \frac{\tau_u \tau_{H,g} H_{rms}^2}{3u_{rms}^2}. \tag{4.5}$$

The calculated values indicate that  $D_{H,g} < 2 \times 10^{-3}$  across all the purely rotating turbulence runs, implying that negative diffusion due to helicity fluctuations is negligible in these simulations. For mean helicity fluctuations  $H$ , even though the correlation time surpasses that of velocity fluctuations, the amplitude of the helicity fluctuations are insufficient to instigate the negative diffusion needed to trigger the dynamo, as predicted by Kraichnan (1976).

### 5. Turbulence in shearing flows

We now turn to the analysis of turbulence in a shearing box. In this section, the Cartesian coordinates in the laboratory frame are denoted by  $(X, Y, Z)$ , and we investigate shearing flows denoted by  $U^{shear} = SXe_y$ . We also include a small yet negative rotation with  $q = -S/\Omega < 0$  to circumvent vorticity dynamos, as discussed in Elperin, Kleeorin & Rogachevskii (2003) and Käpylä *et al.* (2009). Figure 8 presents an  $XY$ -slice of the  $Z$ -component of the vorticity field, revealing the absence of significant large-scale vortices, in contrast to figure 3. Instead, long streaky structures are evident, elongated in the direction of shear, hinting at the presence of stretched vortices aligned with the shear direction. In this section, we will investigate how shear-induced elongation of vortices affects the velocity and helicity fluctuations.

### Correlation time of velocity and kinetic helicity

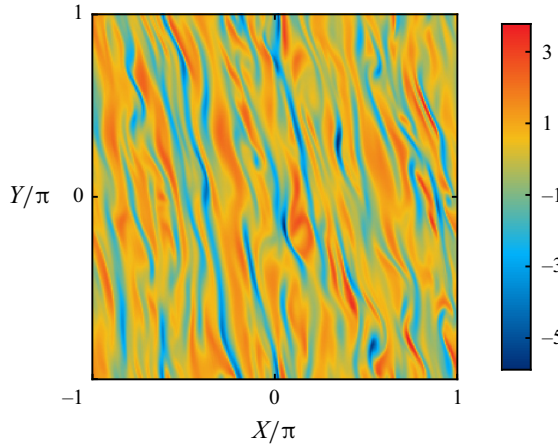


Figure 8. The  $z$  component of the vorticity field (normalized by  $k_f u_{rms}$ ) at the  $z = 0$  slice for run S4 at the end of the simulation.

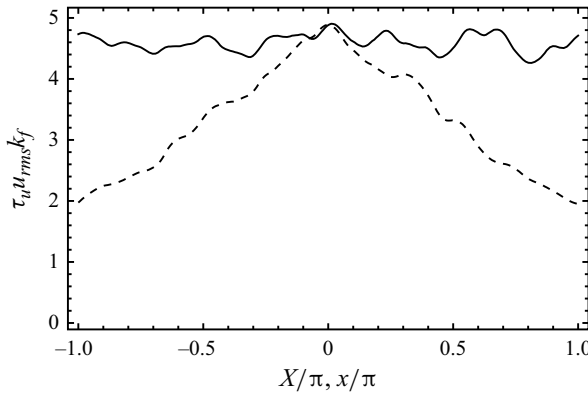


Figure 9. For run S1, correlation times of YZ-averaged velocity auto-correlations in the laboratory frame (dashed) and the shearing frame (solid). Spatial homogeneity is restored in the latter case.

#### 5.1. Shearing box and shearing-frame transformation

The shearing box approximation is commonly used in numerical simulations to study a small patch in a differentially rotating flow whose scale is much smaller than the local curvature of the rotating flow (Goldreich & Lynden-Bell 1965). When considering mean linear shear flows imposed on the turbulent velocity field, the resulting turbulence exhibits inhomogeneity and anisotropy when observed in the laboratory-frame coordinates. In particular, fluid parcels are advected by the background shear flow, making the same-point two-time correlation (3.1)  $\mathcal{T}_u(\tau, \mathbf{X})$  have a shorter correlation time towards the boundary of the box  $X = \pm\pi$ ; see the dashed curve in figure 9.

Such decoherence effect can be removed by exploiting a fundamental symmetry of shearing flows. An observer co-moving with the mean flow velocity  $SX\mathbf{e}_Y$  at location  $\mathbf{X}$  perceives the same turbulent velocity field as an observer in the laboratory frame at the origin. This principle, known as Galilean invariance, ensures the homogeneity of the velocity field in the shearing coordinates  $(x, y, z)$  given by (Sridhar & Subramanian 2009*a,b*)

$$x = X; \quad y = Y - StX; \quad z = Z. \quad (5.1a-c)$$

The general Galilean-invariant time-stationary velocity correlation can be written in the laboratory frame using the symmetry property of shear flow as (see Appendix A)

$$\overline{\mathbf{u}^{lab}(t, \mathbf{X}) \cdot \mathbf{u}^{lab}(t', \mathbf{X}')} = \mathcal{T}_{u,lab}(\mathbf{X} - \mathbf{X}' - S(t - t')X\mathbf{e}_Y, t - t'), \quad (5.2)$$

where overhead bar denotes the time average in our case. This correlation is time stationary but exhibits spatial inhomogeneity along the  $X$ -direction. To address this, we can transform the correlator into the shearing frame, where it becomes spatially homogeneous but loses time stationarity. The latter can only be restored in two special slices in the Fourier space (see below for details). The solid curve in figure 9 shows the velocity correlation time of the  $yz$ -averaged correlators, which restores both spatial homogeneity and time stationarity.

An additional advantage of using the shearing frame is the restoration of normal periodic boundary conditions, allowing for a Fourier transform in the shearwise direction  $\hat{x}$ . Fourier modes in the shearing frame, denoted as  $(k_x, k_y, k_z)$ , are equivalent to shearing-wave modes with wave vectors  $\mathbf{K} = (k_x - St k_y, k_y, k_z)$  in the laboratory frame. It is important to note that there would be no difference in the correlation time of the total kinetic helicity, denoted as  $\tau_H$ , between the two frames. This is due to the fact that  $H(t)$ , being a volume-averaged quantity, remains constant regardless of the frame of reference.

Without further notice, we shall always refer to shearing-frame coordinates by using  $(t, x, y, z)$  in the configuration space and  $(k_x, k_y, k_z)$  in the Fourier space. The helicity density at the shearing-wave vector  $\mathbf{k}$  is given by  $\tilde{g}(\mathbf{k}) = \tilde{\mathbf{u}}^*(\mathbf{k}) \cdot \tilde{\boldsymbol{\omega}}(\mathbf{k})$ , where the vorticity field  $\tilde{\boldsymbol{\omega}} = \mathbf{K}(\mathbf{k}, t) \times \tilde{\mathbf{u}}$  is obtained by first taking the curl of  $\mathbf{u}$  in the laboratory frame, followed by the shearing-frame transformation, and then performing the Fourier transformation.

Sacrificing time stationarity in the Fourier space is unavoidable when reintroducing spatial homogeneity in the shearing frame (see Appendix A). In other words, the unequal-time auto-correlation function  $\langle \tilde{\mathbf{u}}(t + t', \mathbf{k}) \cdot \tilde{\mathbf{u}}(t', \mathbf{k}) \rangle$  not only depends on the time difference  $t$  but also on  $t'$ . This outcome is a general consequence of Galilean invariance (Sridhar & Singh 2014). In Appendix A, it is demonstrated that the correlation functions  $\mathcal{T}_{\tilde{u},\tilde{g}}(t, t', \mathbf{k})$  can maintain stationarity on two two-dimensional slices in Fourier space, i.e.

$$C_{\tilde{u},\tilde{g}}^{I_x}(t, k_y, k_z) \equiv \int \frac{dk_x}{2\pi} \mathcal{T}_{\tilde{u},\tilde{g}}(t, t', \mathbf{k}), \quad (5.3)$$

and

$$C_{\tilde{u},\tilde{g}}^{xz}(t, k_x, k_z) \equiv \mathcal{T}_{\tilde{u},\tilde{g}}(t, t', k_x, k_y = 0, k_z). \quad (5.4)$$

Since inverting  $x \rightarrow -x$  or  $y \rightarrow -y$  is equivalent to  $S \rightarrow -S$  for the correlation functions,  $C_{\tilde{u},\tilde{g}}^{I_x,xz}$  will be invariant under  $(k_x, k_y) \rightarrow (-k_x, -k_y)$ , and so are the corresponding correlation times. We can thus focus ourselves to half of the  $(k_x, k_y)$  plane. Furthermore, the quadratic functions  $C_{\tilde{u},\tilde{g}}^{I_x,xz}$  are also invariant under  $k_z \rightarrow -k_z$ . We therefore only show the results in the  $k_{x,y,z} \geq 0$  planes.

In the upcoming subsection, we present  $\tau_{\tilde{u},\tilde{g}}^{I_x}$  and their corresponding ratios on the  $(k_y, k_z)$  plane. The second quantity (5.4) exclusively involves axisymmetric modes ( $k_y = 0$ ) and, as per the anti-dynamo theorem (Cowling 1933; Zel'dovich 1956), cannot solely induce a dynamo. For a comprehensive view, the  $k_y = 0$  slices (5.4) and the energy densities for both velocity and helicity (corresponding to both quantities (5.3) and (5.4) when  $t = 0$ ) are presented in the supplementary material.

## Correlation time of velocity and kinetic helicity

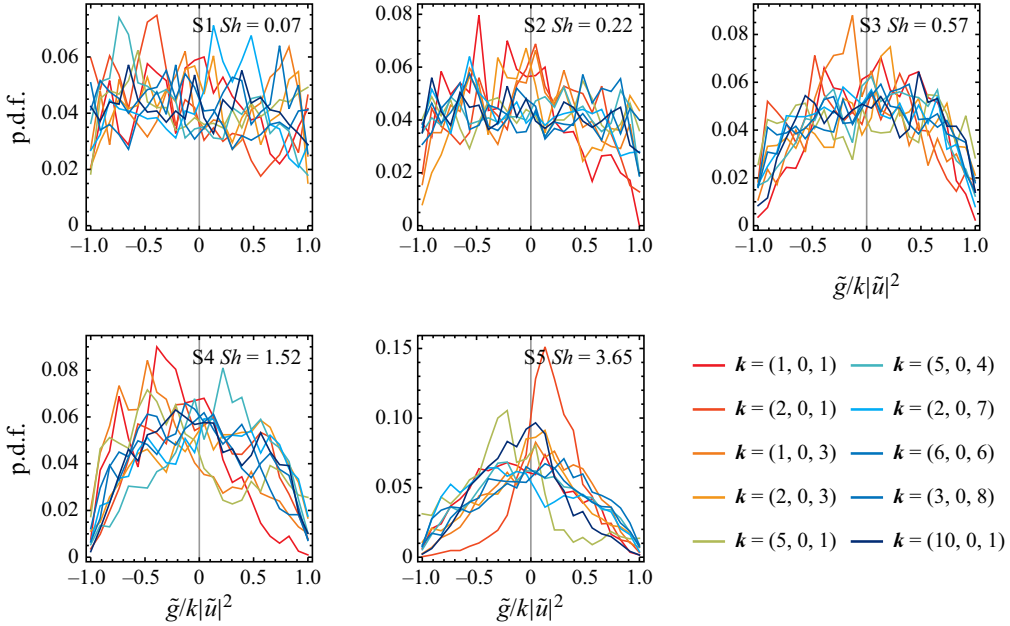


Figure 10. The PDFs of the normalized helicity  $\tilde{g}/k|\tilde{u}|^2$  for a few modes for the shearing-turbulence runs.

### 5.2. Helicity probability distributions

In [figure 10](#) we show 10 typical PDF curves of the normalized helicity modes  $\tilde{g}(\mathbf{k})/k|\tilde{u}|^2$  for each of the runs. At large enough shear rate (runs S4 and S5) and low wavenumbers ( $k < k_f$ ), the PDFs are typically asymmetric with respect to zero, possibly caused by the shear flow. However, the asymmetry is different to those appear in the low-wavenumber modes in purely rotating cases (cf. [figure 7](#)). For the rotating cases, helicity fluctuations appear to be small (i.e. the  $\tilde{g}(\mathbf{k})/k|\tilde{u}|^2$  values are close to zero), with a slight shift of the mean deviating from zero. For the shearing cases, helicity fluctuations with one particular sign are more favoured. In this sense, low-wavenumber modes ( $k < k_f$ ) in shearing turbulence would have stronger helicity fluctuations than those in the rotating turbulence. At large wavenumbers ( $k > k_f$ ), the PDFs becomes symmetric about zero, and runs with lower shear rates (S1 and S2) exhibit flat PDFs, whereas at higher shear rates (S3 to S5), helicity fluctuations demonstrate less extreme values at  $\tilde{g}/k|\tilde{u}|^2 = \pm 1$ , suggesting a decrease in the occurrence of maximally helical fluctuations. This is in contrast to the rotating cases ([figure 7](#)) where high-wavenumber modes still exhibit flat PDFs at large rotation rates.

### 5.3. Results of correlation times

The correlation times for the  $k_x$ -integrated correlation functions (5.3) are presented in [figure 11](#). Unlike cases of rotating turbulence, the instances where  $\tau_{\tilde{g}}/\tau_{\tilde{u}} \geq 1$  are quite limited, with the exception of the most strongly sheared runs, S4 and S5. This trend aligns with the red dashed line in [figure 12](#), illustrating the ratio between the volume-integrated correlation times  $\tau_u$  and  $\tau_g$ . This ratio follows a  $Sh^{0.4}$  scaling and surpasses unity only around  $Sh \simeq 2$ . Simultaneously, the ratio between the correlation time of the total helicity,  $\tau_H$  and  $\tau_u$  exhibits a similar  $Sh$ -dependent scaling but with an overall amplitude exceeding unity. The absence of significant scale separation between velocity and helicity fluctuations

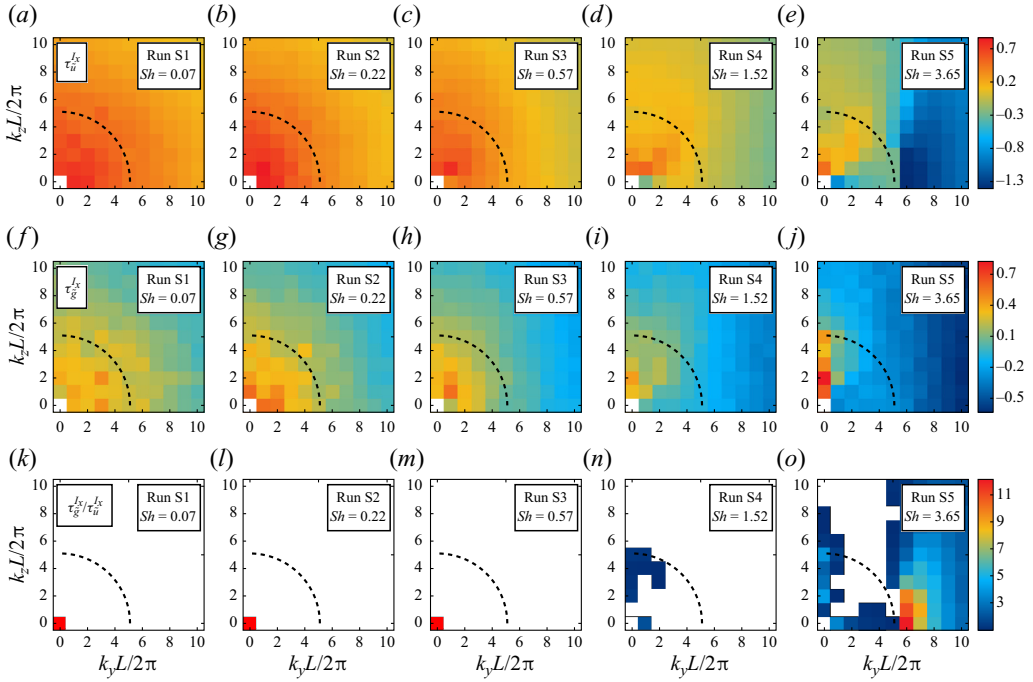


Figure 11. For shearing turbulence, correlation times measured from  $k_x$ -integrated velocity and helicity correlations in the  $(k_y, k_z)$  plane normalized by the eddy turnover time ( $a$ – $e$  and  $f$ – $j$ ,  $\log_{10}$  scale), and their ratios ( $k$ – $o$ , linear scale).

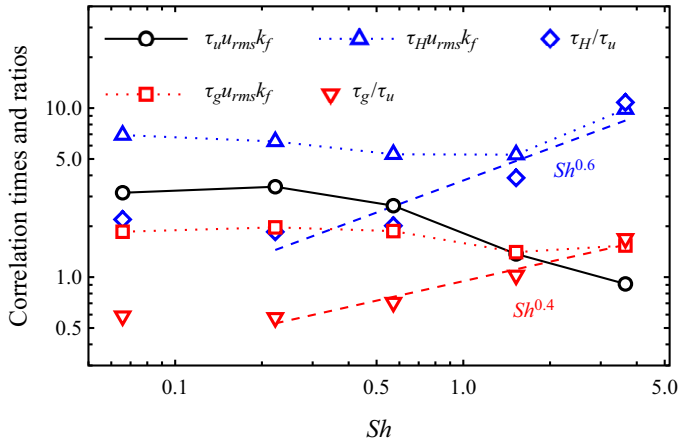


Figure 12. For weakly compressible shearing turbulence, volume-averaged velocity and helicity correlation times and their ratios. The dashed blue and dashed red lines are the fitted power-law relations for  $\tau_H/\tau_u$  and  $\tau_g/\tau_u$ , respectively.

at moderate shear can be ascribed to the elongation of vorticities along the shear direction in shearing flows. Additionally, the lack of distinctive vortex formation, which is observed in rotational flows, contributes to this phenomenon.

The dynamo numbers  $D_{H,g}$  (see (4.5)) computed are less than  $1.7 \times 10^{-3}$ , indicating that there is no negative diffusion in the shearing flows due to the helicity fluctuations.



## Correlation time of velocity and kinetic helicity

Considering the strength of helicity fluctuations and the lack of scale separation at moderate shear, we can conclude that, in the kinematic regime, the helicity fluctuations (incoherent  $\alpha$  mechanism) may not be the possible driver of the shear dynamo simulations.

### 5.4. Shearing burgulence

Burgers' equation is often used as a prototype equation to study turbulence, as it simplifies the Navier–Stokes equations by excluding the pressure gradient term. The form of Burgers' equation that we used to simulate the Burgulence counterpart of the shearing turbulence is given as

$$D_t \mathbf{u} = S u_x \mathbf{e}_y - 2\boldsymbol{\Omega} \times \mathbf{u} + \frac{1}{\rho} \nabla \cdot (2\rho\nu\mathbf{S}) + \mathbf{f}, \quad (5.5)$$

where  $\mathbf{u}$  represents the velocity field,  $S$  is the shear rate and  $\nu$  is the kinematic viscosity. This equation captures essential features of turbulence, such as shock formation and energy dissipation, making it a useful tool for theoretical and numerical studies of turbulent flows.

Theories employing either the second-order correlation approximation or the  $\tau$  approximation closures in the shear-current effect argue for the essential role of the pressure gradient term in the Navier–Stokes equation (Squire & Bhattacharjee 2015b; Zhou & Blackman 2021). Without this term, the required turbulent transport coefficient becomes identically zero. Recent simulations demonstrating shear dynamos in burgulence (Käpylä *et al.* 2022) seemingly challenge the shear-current effect as the primary driver in this context. However, this does not automatically confirm the incoherent  $\alpha$  or helicity fluctuations as the correct explanation. The theoretical and numerical understanding of the role played by the pressure gradient term in the incoherent  $\alpha$  effect is limited, and whether it persists in burgulence remains an open question. In this subsection, we present evidence that the helicity correlation weakens in burgulence, posing a challenge to the efficiency of the incoherent  $\alpha$  effect in this scenario.

To avoid simulation crashes in burgulence runs, it was necessary to increase the viscosity (refer to table 1). This adjustment led to slightly lower Reynolds numbers compared with their counterparts in the Navier–Stokes simulations S1 to S5, but still comparable to those in Käpylä *et al.* (2022).

The correlation times of velocity and helicity in the  $(k_y, k_z)$  plane for shear-burgulence simulations are depicted in figure 13. Comparing the first two rows with their hydrodynamics counterparts in figure 11, we observe that both correlation times decrease more strongly with increasing  $Sh$  in the case of burgulence, especially in the low-wavenumber ( $k < k_f$ ) region. The resulting ratio of the time scales (the third row) shows no substantial scale separation, similar to the shearing hydrodynamic turbulence. The correlation times of volume-averaged correlation functions are presented in figure 14. With increasing  $Sh$ ,  $\tau_u$  decreases at a rate similar to the hydrodynamic case, see figure 12. However, both helicity correlation times  $\tau_{H,g}$  are suppressed more strongly, resulting in lower magnitudes. This leads to much smaller time scale ratios  $\tau_{H,g}/\tau_u$  at  $Sh \gtrsim 1$ .

### 5.5. Keplerian runs

For Keplerian runs, we choose the value  $q = S/\Omega = 3/2$  resulting in a Coriolis number of  $Co = 4Sh/3$ . This case is more representative of astrophysical scenarios, such as in galaxies and accretion disks, where  $q$  can vary from 1 to 2. The methodology applied for these runs remains consistent with the shear runs described in the previous subsection.

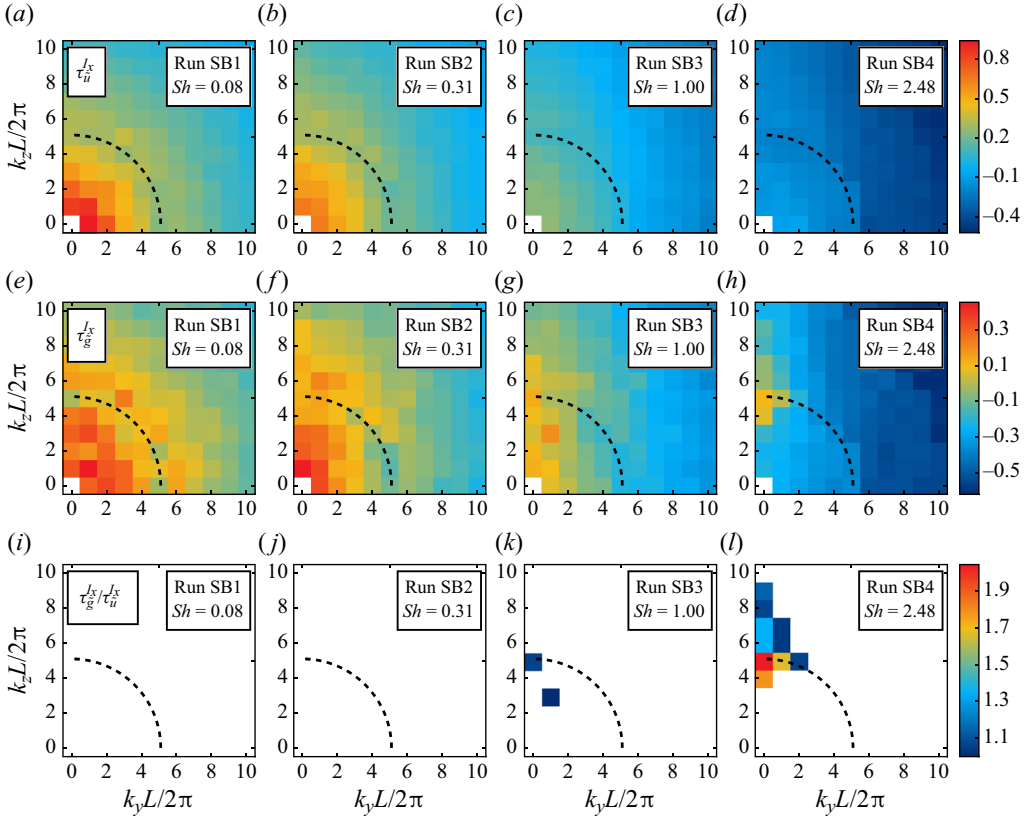


Figure 13. For shearing Burgulence, correlation times measured from  $k_x$ -integrated velocity and helicity correlations in the  $(k_y, k_z)$  plane and normalized by the eddy turnover time (a–d and e–h, log<sub>10</sub> scale), and their ratios (i–h, linear scale).

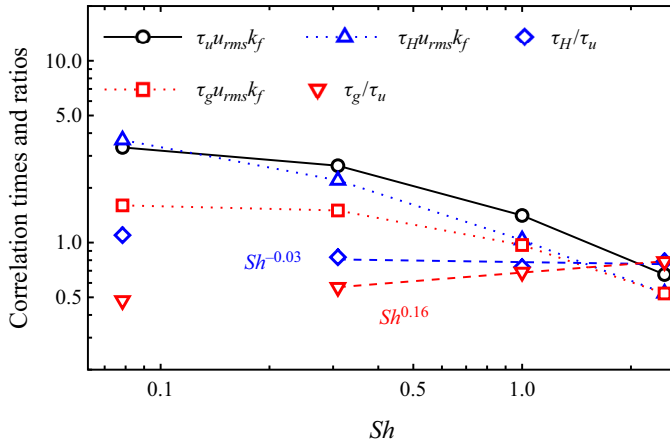


Figure 14. Volume-averaged velocity and helicity correlation times and their ratios for the shearing Burgulence cases. The dashed blue and dashed red lines are the fitted power-law relations for  $\tau_H / \tau_u$  and  $\tau_g / \tau_u$ , respectively.

Correlation time of velocity and kinetic helicity

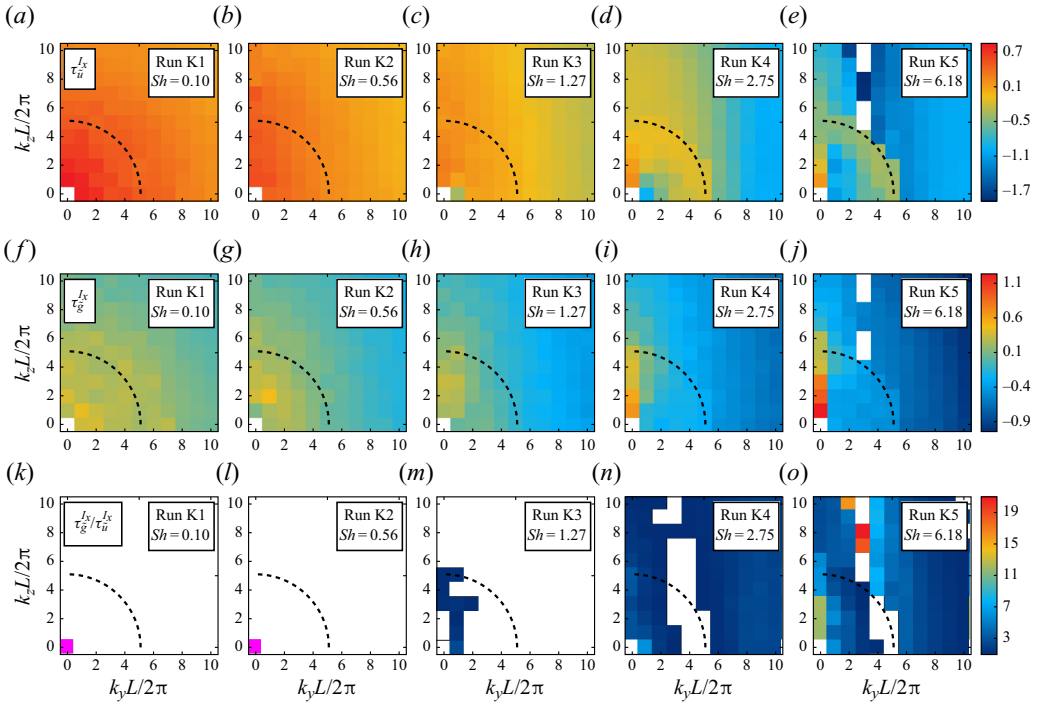


Figure 15. For Keplerian turbulence, correlation times measured from the  $k_x$ -integrated velocity and helicity correlations in the  $(k_y, k_z)$  plane and normalized by the eddy turnover time ( $a-e$  and  $f-j$ , log<sub>10</sub> scale), and their ratios ( $k-o$ , linear scale).

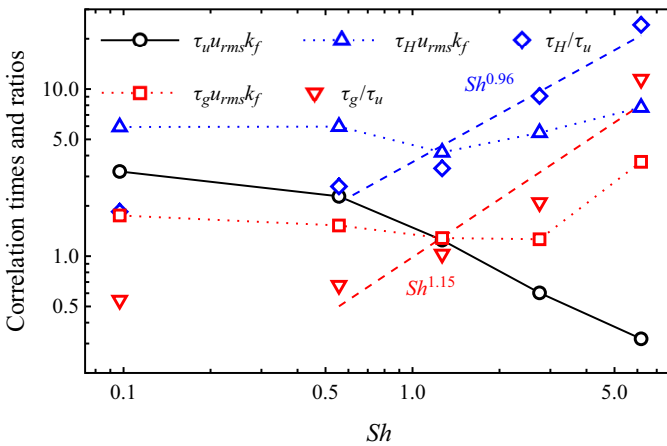


Figure 16. For weakly compressible Keplerian turbulence, volume-averaged velocity and helicity correlation times and their ratios. The dashed blue and dashed red lines are the fitted power-law relations for  $\tau_H/\tau_u$  and  $\tau_g/\tau_u$ , respectively.

In figure 15, Fourier space results reveal a more distinct scale separation compared with both the shearing turbulence (figure 11) and shearing burgulence (figure 13) cases. This enhanced separation is attributed to the additional rotation, known to form condensate through inverse cascade producing large-scale vortices. This time-scale separation persists despite the elongation effect of the vortices in the direction of the shear. The volume-integrated time scales shown in figure 16 also display a larger-scale

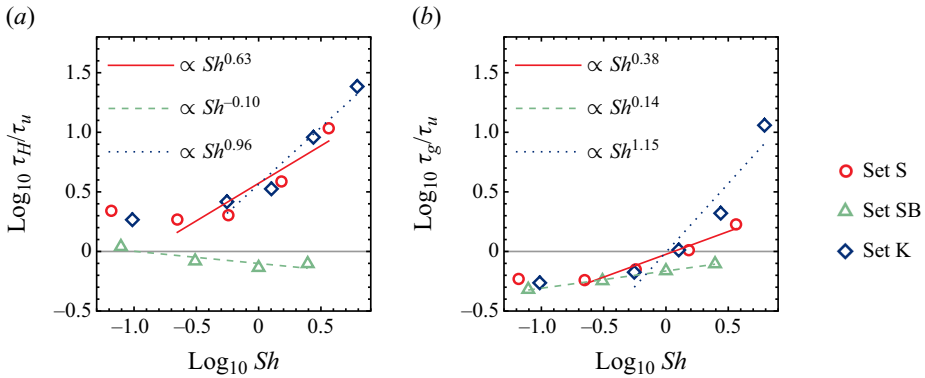


Figure 17. Ratios of time scales  $\tau_{H,g}/\tau_u$  for different sets of runs: shearing turbulence (S), shearing burgulence (SB) and Keplerian turbulence (K). Datasets are the same as those in figures 12, 14 and 16.

separation: the magnitudes of both ratios,  $\tau_{H,g}/\tau_u$  are similar to the shearing cases (cf. figure 12) at  $Sh = 0.5$ . However, their scalings with  $Sh$  become much stronger, with  $\tau_H/\tau_u \propto Sh^{0.96}$  and  $\tau_g/\tau_u \propto Sh^{1.15}$ . Interestingly, these power-law indices are larger than either purely rotating ( $\propto Co_f^{0.85}$  and  $\propto Co_f^{0.09}$ , respectively) or purely shearing (with weak counter-rotation,  $\propto Sh^{0.63}$  and  $\propto Sh^{0.38}$ , respectively) cases, revealing a constructive collaboration of the rotation and the shear flow.

In these Keplerian runs, we also find that the dynamo number  $D_{H,g}$  (see (4.5)) is less than  $1.5 \times 10^{-3}$ , suggesting that the strength of helicity fluctuations is relatively weak. It is important to note that this strength depends on the Mach number of the flows, which in our simulations is around 0.1. The strength of these helicity fluctuations could increase with higher Mach numbers. Therefore, further exploration of this effectiveness on the dynamo mechanism in different flow regimes, such as transonic and supersonic flows more relevant to astrophysical scenarios, would be of significant interest. However, such an investigation is beyond the scope of the current work.

### 6. Comparison with previous shear dynamo simulations

In the previous sections we have obtained the degree of time-scale separation between helicity and velocity fluctuations in rotating, shearing and Keplerian hydrodynamic turbulence, as well as in shearing burgulence. In this section we compare our parameter space with those in previous numerical simulations of large-scale dynamos in shear flows and seek the implications in the light of figures 6, 12, 14 and 16. We note that these results are obtained in weakly compressible flows at  $Ma \sim 0.1$ , and the scaling indices could change with increasing compressibility.

The general idea we gained from the previous section is that the time-scale separation between helicity and velocity fluctuations increases with increasing rotation or shear rate. This increase is quantified using  $\zeta = \tau_{H,g}/\tau_u$ , and we present all the results of  $\zeta$  for the runs with shear in figure 17 to facilitate comparison. The renovating-flow model in Jingade & Singh (2021) suggests that there exists a critical value  $\zeta_{crit}$  ( $= 3$  in their work) above which the incoherent  $\alpha$  effect is capable of driving a shear dynamo. The exact value of  $\zeta_{crit}$  in hydrodynamical or magnetohydrodynamical turbulence might be different from 3, given the simplifications made in the model, but it is reasonable to expect the existence of some  $\zeta_{crit} > 1$ , since the coherent effect has to be strong enough to overcome

turbulent dissipation. Combining that (i)  $\zeta$  increases with increasing  $Sh$  and (ii)  $\zeta_{crit} > 1$ , it follows that the incoherent  $\alpha$  effect requires a critical value of  $Sh$ .

A critical shear rate is also predicted in the alternative explanation of shear dynamos, the shear-current effect, but there is an important distinction regarding its scale dependence. The shear-current effect model predicts the dynamo growth rate for the  $xy$ -averaged field to be (see e.g. Zhou & Blackman 2021)

$$\gamma = \left[ \frac{(\beta_{xx} - \beta_{yy})^2}{4} k_1^4 + \beta_{xy} \beta_{yx} k_1^4 + S \beta_{yx} k_1^2 \right]^{1/2} - \frac{\beta_{xx} + \beta_{yy}}{2} k_1^2, \quad (6.1)$$

where  $\beta_{ij}$  is the magnetic turbulent diffusivity tensor (which depends on  $Sh$ ), and  $k_1$  is the wavenumber of the large-scale magnetic field of interest. Considering the simplified case where  $\beta_{xx} = \beta_{yy} = \beta_0$  and  $\beta_{xy} = 0$ , we have

$$\gamma = \sqrt{S \beta_{yx} k_1^2 - \beta_0 k_1^2} = -\beta_0 \left( k_1 - \frac{\sqrt{S \beta_{yx}}}{2 \beta_0} \right)^2 + \frac{S \beta_{yx}}{4 \beta_0}. \quad (6.2)$$

The first equality implies that a minimal shear rate is required for the growth rate to be positive. However, the second equality shows that the dynamo growth rate remains finite for any small  $Sh$ , as long as the mode with the fastest growth rate fits into the simulation box. This contrasts with the incoherent  $\alpha$  effect, which requires a critical shear rate  $Sh_{crit}$  for maximum growth, even when  $k_1$  corresponds to the fastest growing mode. This distinction can help differentiate between these two dynamo mechanisms.

Yousef *et al.* (2008) investigated the shear dynamo problem in the kinematic phase using tall simulation boxes, low shear rates and without rotation. In their study, the vertical scales of the simulation domain are always larger than the typical scales of the large-scale magnetic fields, allowing the fastest growing mode to be captured. They used a dimensionless shear parameter  $Sh \lesssim 1/(3\pi) \simeq 0.1$  based on our definition. All simulations in their study exhibited shear dynamos, even at very low values of  $Sh$  (notably, for  $Sh \gtrsim 0.05$ , the large-scale fields are disrupted in the nonlinear stage; see Teed & Proctor 2016). Therefore, combining our results on the threshold shear needed to bring in the time-scale separation with the findings from Yousef *et al.* (2008) suggests that the observed shear dynamos are unlikely to be driven by the incoherent  $\alpha$  effect.

It is also worth noting that both Yousef *et al.* (2008) and Teed & Proctor (2016) used  $Re = Rm \simeq 5$ , which is sub-critical for a small-scale dynamo. Hence, their simulations fall outside the realm of the magnetic shear-current effect, which requires strong magnetic fluctuations (Squire & Bhattacharjee 2015*b*). Furthermore, the kinetic shear-current effect (Rogachevskii & Kleeorin 2003) is also likely ruled out because the steep kinetic energy spectrum at such low  $Re$  is unfavourable for the shear dynamo (Zhou & Blackman 2021). Given that the current study also disfavours the incoherent  $\alpha$  driver, it becomes puzzling what drives large-scale dynamos in non-helical shearing turbulence when both the Reynolds and magnetic Reynolds numbers are not very large. This suggests a need for further investigation into the properties of shear dynamos, potentially leading to a new classification based on these properties.

As for large-scale dynamos in shearing turbulence, Käpylä *et al.* (2020) explored cases with  $Sh = 1.6$  and  $(Re, Rm) \simeq (0.5, 2)$  and  $(Re, Rm) \simeq (0.7, 12)$ . By using the nonlinear test-field method, they ruled out the shear-current effect as the driver of the shear dynamo. In the current study, we find that the time-scale separation between the velocity and helicity fluctuations is strongly suppressed in shearing turbulence compared with its

hydrodynamic counterpart (i.e. the S and SB runs in [figure 17](#)). This result seemingly suggests the incapability of the incoherent  $\alpha$  effect with the Burgers equation. However, we cannot rule out the possibility that the critical ratio between time scales  $\tau_{H,g}/\tau_u$  needed for a shear dynamo in shearing burgulence is lower than that in the hydrodynamic case.

The consideration of shearing burgulence also raises the important question of the Mach number dependence of  $\zeta$  in rotating or shearing flows. The current study only explored weakly compressible hydrodynamical turbulence at  $Ma \simeq 0.1$ . For turbulence in accretion disks, the Mach number depends on the Shakura–Sunyaev viscosity parameter  $\alpha_{SS}$ , with  $Ma \simeq \alpha_{SS}^{1/2}$  (Blackman 1998). In moderately compressible flows, helicity fluctuations might become stronger, potentially allowing the dynamo number to cross the threshold of the incoherent  $\alpha$  effect. Investigating how time-scale separation and helicity fluctuation amplitudes vary with  $Ma$  could provide valuable insights into the dynamo problem in accretion disks.

## 7. Conclusions

In this investigation, we scrutinized the correlation times of velocity and helicity fluctuations in diverse fluid flow scenarios, including rotating flows, shearing flows, Keplerian flows and shearing burgulence. Our primary objective is to gauge the correlation time between velocity and helicity fluctuations, crucial for elucidating the kinematic dynamo mechanisms in non-helical turbulent flows. While both the shear-current effect and helicity fluctuations are leading candidates for explaining shear dynamos, we focused specifically on the latter in this study.

We have investigated the correlation times for individual Fourier modes as well as for volume-averaged values, each used in different theories. In the context of rotating flows, a notable temporal separation between velocity and helicity fluctuations is revealed, particularly prominent in large-scale modes influenced by the Coriolis force arising from rotation. In Fourier space ([figure 5](#)), an increase in the rotation rate results in an overall elevation of the magnitudes of time-scale ratios and a greater number of modes where this ratio surpasses unity. These modes are preferentially situated along the rotation axis, particularly noticeable in smaller scales with wavenumbers close to, but surpassing, the forcing wavenumber. On the other hand, the magnitudes of both velocity and helicity correlation time scales decreases when the rotation rate increases. This prolonged persistence of helicity fluctuations relative to velocity fluctuations is ascribed to the formation of cyclonic and anti-cyclonic vortices within the rotating turbulence.

In shearing cases (with weak negative rotation to suppress the vorticity dynamo), non-axisymmetric modes conducive to dynamos exhibited more coherent helicity fluctuations only in strongly sheared flows ( $Sh \simeq 2$ , [figure 11](#)). The lack of the required scale separation for helicity and velocity fluctuations in non-axisymmetric modes that is crucial for dynamo initiation was linked to vortex elongation along the shear direction. Therefore, we infer that helicity fluctuations may not be the driving force for shearing dynamos in non-rotating shearing flows, necessitating a re-evaluation or further categorization of shear dynamos based on their properties. For Keplerian flows, time-scale separation in non-axisymmetric modes is observed at moderate shear rates ( $Sh \gtrsim 1$ , [figure 15](#)), which suggests that helicity fluctuations may play a more significant role since the shear-current effect is suppressed (Zhou & Blackman 2021).

Furthermore, the shear-current effect is estimated to vanish in shearing burgulence (Squire & Bhattacharjee 2016; Zhou & Blackman 2021). Our results imply that removing the pressure gradient in the Navier–Stokes equation introduces a decoherence effect to



helicity, challenging the incoherent  $\alpha$  effect (figure 13). Consequently, the driver for large-scale dynamos in shearing turbulence remains elusive.

An essential consideration for dynamos is the strength of helicity fluctuations. In our study, conducted for subsonic flows with Mach numbers  $\simeq 0.1$ , the normalized ratio of helicity fluctuations to velocity fluctuations, as expressed in (4.5), remained below  $2 \times 10^{-3}$ . Such weak fluctuations raise doubts about triggering dynamos, even in Keplerian runs. Considering the dependence on the fourth power of velocity in the numerator and quadratic power in the denominator, an extension of this study to transonic or supersonic cases with higher Mach numbers could significantly increase fluctuation strength, potentially leading to large-scale dynamos. This extension may hold implications for accretion disk dynamos.

**Supplementary material.** Supplementary material is available at <https://doi.org/10.1017/jfm.2024.1006>.

**Acknowledgements.** We thank the anonymous referees for their constructive suggestions which help improve the paper. We thank A. Brandenburg, J. Schober and A. Roper Pol for their help in developing the numerical methods. We also thank A. Brandenburg, E.G. Blackman and M. Rheinhardt for insightful discussions. Nordita is partially supported by Nordforsk. We acknowledge the allocation of computing resources provided by the Swedish National Allocations Committee at the Center for Parallel Computers at the Royal Institute of Technology in Stockholm and Linköping. Part of the numerical simulations were carried out on the Siyuan Mark-I and the ARM platform clusters supported by the Center for High Performance Computing at Shanghai Jiao Tong University, and the Astro cluster supported by Tsung-Dao Lee Institute. N.J. acknowledges the use of the High Performance Computing (HPC) resources made available by the Computer Centre of the Indian Institute of Astrophysics (IIA).

**Funding.** H.Z. acknowledges support from grant number 2023M732251 from the China Postdoctoral Science Foundation.

**Declaration of interests.** The authors report no conflict of interest.

**Data availability.** The data that support the findings of this study will be shared on reasonable request to the authors.

**Author ORCIDs.**

 Hongzhe Zhou <https://orcid.org/0000-0002-2991-5306>;

 Naveen Jingade <https://orcid.org/0000-0002-8079-9566>.

## Appendix A. Time stationarity in Fourier space

Consider a Cartesian frame with coordinates  $(X, Y, Z)$ , where the shear flow is denoted by  $U^{shear} = SXe_Y$ . In the laboratory frame, the most general form of a two-point unequal-time auto-correlation function can be derived using Galilean invariance (Sridhar & Singh 2014). This invariance is associated with measurements made by observers whose velocity, relative to the laboratory frame  $(t, \mathbf{X})$  matches that of the background shear flow. These comoving observers can be characterized by  $\boldsymbol{\xi} = (\xi_1, \xi_2, \xi_3)$ , representing the position of the origin of the comoving observer at the initial time zero. The position of the origin of the comoving observer at time  $t$  is given by

$$\mathbf{X}_c(t, \boldsymbol{\xi}) = (\xi_1, \xi_2 + St\xi_1, \xi_3). \quad (\text{A1})$$

Since the statistics of the velocity field remain the same, the velocity correlator measured in the laboratory frame or the corresponding comoving frame must be the same, and can

be expressed as

$$\overline{\mathbf{u}^{lab}(t, \mathbf{X}) \cdot \mathbf{u}^{lab}(t', \mathbf{X}')} = \overline{\mathbf{u}^{lab}(t, \mathbf{X} + \mathbf{X}_c(\boldsymbol{\xi}, t)) \cdot \mathbf{u}^{lab}(t', \mathbf{X}' + \mathbf{X}_c(\boldsymbol{\xi}, t'))}. \quad (\text{A2})$$

The Navier–Stokes equation does not explicitly depend on time, indicating that the velocity statistics must be time stationary. Consequently, a Galilean-invariant velocity correlator with an arbitrary time shift  $t_0$  can be expressed as

$$\begin{aligned} \overline{\mathbf{u}^{lab}(t, \mathbf{X}) \cdot \mathbf{u}^{lab}(t', \mathbf{X}')} \\ = \overline{\mathbf{u}^{lab}(t + t_0, \mathbf{X} + \mathbf{X}_c(\boldsymbol{\xi}, t + t_0)) \cdot \mathbf{u}^{lab}(t' + t_0, \mathbf{X}' + \mathbf{X}_c(\boldsymbol{\xi}, t' + t_0))}. \end{aligned} \quad (\text{A3})$$

This equation holds for any arbitrary  $\boldsymbol{\xi}$  and time  $t_0$ . By choosing  $\boldsymbol{\xi} = -\mathbf{X}'$  and  $t_0$  as  $-t'$ , we obtain the most general form of the correlator as follows:

$$\overline{\mathbf{u}^{lab}(t, \mathbf{X}) \cdot \mathbf{u}^{lab}(t', \mathbf{X}')} = \mathcal{T}_{u,lab}(\mathbf{X} - \mathbf{X}' - S(t - t')\mathbf{X}\mathbf{e}_Y, t - t'). \quad (\text{A4})$$

While  $\mathcal{T}_{u,lab}$  is time stationary, it explicitly depends on  $\mathbf{X}$ , and is therefore inhomogeneous in space. This characteristic is akin to the velocity correlator that would result from applying the Taylor hypothesis to frozen turbulence.

In a shearing-frame transformation, a set of Cartesian coordinates  $(x, y, z)$  whose directions are parallel to those of the laboratory frame is linked to the laboratory-frame coordinates by

$$\mathbf{x} = \mathbf{X} - St\mathbf{X}\mathbf{e}_Y, \quad (\text{A5})$$

and the velocity field in the shearing frame is defined by

$$\mathbf{u}(t, \mathbf{x}) = \mathbf{u}(t, \mathbf{X} - St\mathbf{X}\mathbf{e}_Y) = \mathbf{u}^{lab}(t, \mathbf{X}). \quad (\text{A6})$$

Applying the transformation to (A4) yields

$$\overline{\mathbf{u}(t, \mathbf{x}) \cdot \mathbf{u}(t', \mathbf{x}')} = \mathcal{T}_u(\mathbf{x} - \mathbf{x}' + St'(\mathbf{x} - \mathbf{x}')\mathbf{e}_Y, t - t'), \quad (\text{A7})$$

which restores spatial homogeneity at the cost of time stationarity when  $\mathbf{x} \neq \mathbf{x}'$ .

To measure the correlation time in Fourier space, we require the velocity correlator to be both spatially homogeneous and time stationary. Thus, we aim to construct a correlator that preserves both of these properties. With the shearing transformation for the spatial coordinate, we can derive the corresponding transformation for its Fourier counterpart. This transformation is obtained from the conservation of the phase of the wave,  $\mathbf{K} \cdot \mathbf{X} = \mathbf{k} \cdot \mathbf{x}$  (see the Appendix in Sridhar & Singh 2010, for details), where  $\mathbf{K}$  is the laboratory-frame wavevector and  $\mathbf{k}$  is the shearing-frame wavevector. Using (A5), we find  $\mathbf{K} = \mathbf{k} - Stk_y\hat{\mathbf{X}}$ .

The spatial homogeneity of (A7) ensures  $\overline{\tilde{\mathbf{u}}^*(t, \mathbf{k}) \cdot \tilde{\mathbf{u}}(t', \mathbf{k}')} = 0$  unless  $\mathbf{k} = \mathbf{k}'$ . Consequently, we can define

$$\mathcal{T}_{\tilde{u}}(t, t', \mathbf{k}) = \overline{\tilde{\mathbf{u}}^*(t, \mathbf{k}) \cdot \tilde{\mathbf{u}}(t', \mathbf{k})}, \quad (\text{A8})$$

whose general form is given by Fourier transforming (A7),

$$\begin{aligned} \mathcal{T}_{\tilde{u}}(t, t', \mathbf{k}) &= \int d^3r e^{-i\mathbf{k} \cdot \mathbf{r}} \mathcal{T}_u(\mathbf{r} + St'r_x\mathbf{e}_Y, t - t'); \quad \text{where } \mathbf{r} = \mathbf{x} - \mathbf{x}' \\ &= \tilde{\mathcal{T}}_u(\mathbf{k} - St'k_y\hat{\mathbf{X}}, t - t'). \end{aligned} \quad (\text{A9})$$

Note that the Fourier space correlator  $C_{\tilde{u}}(t, t', \mathbf{k})$  is not time stationary, given its explicit dependence on the time  $t'$ . The time-stationary property is crucial for building statistics

## Correlation time of velocity and kinetic helicity

over time, facilitating the averaging required to obtain the correlator. Consequently, we opt for specific correlators constructed from (A9), designed to preserve the time-stationary property.

Firstly if we restrict ourselves to the  $k_y = 0$  plane, we obtain a set of correlator that are time stationary, denoted as

$$C_{\tilde{u}}^{xz}(t, t', k_x, k_z) = \mathcal{T}_{\tilde{u}}(t, t', k_x, k_y = 0, k_z) = \tilde{\mathcal{T}}_{\tilde{u}}(k_x, 0, k_z, t - t'). \quad (\text{A10})$$

The other set is obtained by integrating the correlator (A9), over  $k_x$ . By applying the transformation property of Fourier wave vectors, the integrals of the correlators can be expressed as

$$\int dk_x dk_y \tilde{\mathcal{T}}_{\tilde{u}}(k_x - St'k_y, k_y, k_z, t - t') = \int dK_x dK_y \tilde{\mathcal{T}}_{\tilde{u}}(K_x, K_y, k_z, t - t'), \quad (\text{A11})$$

where  $K_x = k_x - St'k_y$  and  $K_y = k_y$  and the Jacobian of the transformation between laboratory-frame and shearing-frame wavevectors is unity. Defining a correlator by integrating over the  $K_x$  wavevector

$$C_{\tilde{u}}^{Ix}(t, t', k_y, k_z) = \int \frac{dK_x}{2\pi} \tilde{\mathcal{T}}_{\tilde{u}}(K_x, k_y, k_z, t - t'), \quad (\text{A12})$$

we obtain the time-stationary correlation function, as they depend only on the difference in time ( $t - t'$ ).

We can express the integrated correlator (A12) in terms of the velocity as

$$\begin{aligned} C_{\tilde{u}}^{Ix}(t, t', k_y, k_z) &= \int \frac{dk_x}{2\pi} \overline{\tilde{\mathbf{u}}^*(k_x, k_y, k_z, t) \cdot \tilde{\mathbf{u}}(k_x, k_y, k_z, t')} \\ &= \int dx \overline{\mathbf{u}^*(x, k_y, k_z, t) \cdot \mathbf{u}(x, k_y, k_z, t')}, \end{aligned} \quad (\text{A13})$$

where the last equality is due to the application of Parseval's theorem in one dimension. In our numerical experiments, we approximate the last expression by integrating  $x$  in the range  $-5\pi/32 \leq x \leq 5\pi/32$ , which captures the small-scale modes responsible for the dynamo transport coefficients. The compromise of integrating over a limited range of  $x$  is made because the two-time correlators have to be calculated from the Fourier modes during the post-processing, and the output modes are limited due to the high cadence needed to capture short correlation times.

It is crucial to highlight that (A10) provides the axisymmetric modes, while (A12) yields the non-axisymmetric modes in an integrated form along one dimension. The significance lies in the fact that only the non-axisymmetric modes contribute to dynamos, making them particularly relevant for dynamo studies.

## REFERENCES

- ALEXAKIS, A. 2015 Rotating Taylor-Green flow. *J. Fluid Mech.* **769**, 46–78.
- BALBUS, S.A. & HAWLEY, J.F. 2006 An exact, three-dimensional, time-dependent wave solution in local Keplerian flow. *Astrophys. J.* **652** (2), 1020–1027.
- BARTELLO, P., METAIS, O. & LESIEUR, M. 1994 Coherent structures in rotating three-dimensional turbulence. *J. Fluid Mech.* **273**, 1–29.
- BLACKMAN, E.G. 1998 Variability associated with alpha accretion disc theory for standard and advection-dominated discs. *Mon. Not. R. Astron. Soc.* **299** (4), L48–L52.
- BLACKMAN, E.G. & FIELD, G.B. 2002 New dynamical mean-field dynamo theory and closure approach. *Phys. Rev. Lett.* **89** (26), 265007.

- BRANDENBURG, A. 2001 The inverse cascade and nonlinear alpha-effect in simulations of isotropic helical hydromagnetic turbulence. *Astrophys. J.* **550** (2), 824–840.
- BRANDENBURG, A. 2005 The case for a distributed solar dynamo shaped by near-surface shear. *Astrophys. J.* **625** (1), 539–547.
- BRANDENBURG, A., RÄDLER, K.H., RHEINHARDT, M. & KÄPYLÄ, P.J. 2008 Magnetic diffusivity tensor and dynamo effects in rotating and shearing turbulence. *Astrophys. J.* **676** (1), 740–751.
- BRANDENBURG, A. & SUBRAMANIAN, K. 2005a Astrophysical magnetic fields and nonlinear dynamo theory. *Phys. Rep.* **417** (1–4), 1–209.
- BRANDENBURG, A. & SUBRAMANIAN, K. 2005b Minimal tau approximation and simulations of the alpha effect. *Astron. Astrophys.* **439** (3), 835–843.
- CHEN, S. & KRAICHNAN, R.H. 1989 Sweeping decorrelation in isotropic turbulence. *Phys. Fluids A* **1** (12), 2019–2024.
- CLARK DI LEONI, P., COBELLI, P.J. & MININNI, P.D. 2015 The spatio-temporal spectrum of turbulent flows. *Eur. Phys. J. E* **38** (12), 1–10.
- COWLING, T.G. 1933 The magnetic field of sunspots. *Mon. Not. R. Astron. Soc.* **94**, 39–48.
- DALLAS, V. & TOBIAS, S. 2018 Rotationally induced coherence in turbulent kinematic dynamos. [arXiv:1805.02291](https://arxiv.org/abs/1805.02291)
- DITTRICH, P., MOLCHANOV, S.A., SOKOLOV, D.D. & RUZMAIKIN, A.A. 1984 Mean magnetic field in renovating random flow. *Astron. Nachr.* **305**, 119–125.
- ELPERIN, T., KLEEORIN, N. & ROGACHEVSKII, I. 2003 Generation of large-scale vorticity in a homogeneous turbulence with a mean velocity shear. *Phys. Rev. E* **68** (1), 016311.
- FAVIER, B., GODEFERD, F.S. & CAMBON, C. 2010 On space and time correlations of isotropic and rotating turbulence. *Phys. Fluids* **22** (1), 015101.
- FEDOTOV, S., BASHKIRTSEVA, I. & RYASHKO, L. 2006 Stochastic dynamo model for subcritical transition. *Phys. Rev. E* **73** (6), 066307.
- GILBERT, A.D. & BAYLY, B.J. 1992 Magnetic field intermittency and fast dynamo action in random helical flows. *J. Fluid Mech.* **241**, 199–214.
- GOLDREICH, P. & LYNDEN-BELL, D. 1965 II. Spiral arms as sheared gravitational instabilities. *Mon. Not. R. Astron. Soc.* **130**, 125.
- HEINEMANN, T., MCWILLIAMS, J.C. & SCHEKOCHIHIN, A.A. 2011 Large-scale magnetic field generation by randomly forced shearing waves. *Phys. Rev. Lett.* **107** (25), 255004.
- HOYNG, P. 1987 Turbulent transport of magnetic fields. Part 2. The role of fluctuations in kinematic theory. *Astron. Astrophys.* **171**, 357.
- HOYNG, P. 1988 Turbulent transport of magnetic fields. III. Stochastic excitation of global magnetic modes. *Astrophys. J.* **332**, 857.
- JINGADE, N. & SINGH, N.K. 2020 Mean field dynamo action in shear flows. I. Fixed kinetic helicity. *Mon. Not. R. Astron. Soc.* **495** (4), 4557–4569.
- JINGADE, N. & SINGH, N.K. 2021 Mean field dynamo action in shearing flows. II. Fluctuating kinetic helicity with zero mean. *Mon. Not. R. Astron. Soc.* **508** (4), 5163–5175.
- JINGADE, N., SINGH, N.K. & SRIDHAR, S. 2018 Generation of large-scale magnetic fields due to fluctuating in shearing systems. *J. Plasma Phys.* **84** (6), 735840601.
- KÄPYLÄ, M.J., RHEINHARDT, M. & BRANDENBURG, A. 2022 Compressible test-field method and its application to shear dynamos. *Astrophys. J.* **932** (1), 8.
- KÄPYLÄ, M.J., VIZOSO, J.Á., RHEINHARDT, M., BRANDENBURG, A. & SINGH, N.K. 2020 On the existence of shear-current effects in magnetized turbulence. *Astrophys. J.* **905** (2), 179.
- KÄPYLÄ, P.J., MITRA, D. & BRANDENBURG, A. 2009 Numerical study of large-scale vorticity generation in shear-flow turbulence. *Phys. Rev. E* **79** (1), 016302.
- KLEEORIN, N. & ROGACHEVSKII, I. 2008 Mean-field dynamo in a turbulence with shear and kinetic helicity fluctuations. *Phys. Rev. E* **77** (3), 036307.
- KRAICHNAN, R.H. 1967 Inertial ranges in two-dimensional turbulence. *Phys. Fluids* **10** (7), 1417–1423.
- KRAICHNAN, R.H. 1976 Diffusion of weak magnetic fields by isotropic turbulence. *J. Fluid Mech.* **75**, 657–676.
- MITRA, D. & BRANDENBURG, A. 2012 Scaling and intermittency in incoherent  $\alpha$ -shear dynamo. *Mon. Not. R. Astron. Soc.* **420** (3), 2170–2177.
- MOFFATT, H.K. 1978 *Magnetic Field Generation in Electrically Conducting Fluids*. Cambridge Monographs on Mechanics and Applied Mathematics. Cambridge University Press.
- NEWTON, A.P.L. & KIM, E.-J. 2012 Effect of stochasticity in mean field dynamo models. *Phys. Plasmas* **19** (7), 072310.
- PARKER, E.N. 1955 Hydromagnetic dynamo models. *Astrophys. J.* **122**, 293.

- PENCIL CODE COLLABORATION, *et al.* 2021 The Pencil Code, a modular MPI code for partial differential equations and particles: multipurpose and multiuser-maintained. *J. Open Source Softw.* **6** (58), 2807.
- PIPIN, V.V. 2008 The mean electro-motive force and current helicity under the influence of rotation, magnetic field and shear. *Geophys. Astrophys. Fluid Dyn.* **102** (1), 21–49.
- POUQUET, A., FRISCH, U. & LEORAT, J. 1976 Strong MHD helical turbulence and the nonlinear dynamo effect. *J. Fluid Mech.* **77**, 321–354.
- PROCTOR, M.R.E. 2007 Effects of fluctuation on  $\alpha\Omega$  dynamo models. *Mon. Not. R. Astron. Soc.* **382** (1), L39–L42.
- RÄDLER, K.-H. & STEPANOV, R. 2006 Mean electromotive force due to turbulence of a conducting fluid in the presence of mean flow. *Phys. Rev. E* **73** (5), 056311.
- RHEINHARDT, M. & BRANDENBURG, A. 2010 Test-field method for mean-field coefficients with MHD background. *Astron. Astrophys.* **520**, A28.
- RICHARDSON, K.J. & PROCTOR, M.R.E. 2012 Fluctuating  $\alpha\Omega$  dynamos by iterated matrices. *Mon. Not. R. Astron. Soc.* **422** (1), L53–L56.
- ROGACHEVSKII, I. & KLEEORIN, N. 2003 Electromotive force and large-scale magnetic dynamo in a turbulent flow with a mean shear. *Phys. Rev. E* **68** (3), 036301.
- ROGACHEVSKII, I. & KLEEORIN, N. 2004 Nonlinear theory of a ‘shear-current’ effect and mean-field magnetic dynamos. *Phys. Rev. E* **70** (4), 046310.
- RÜDIGER, G. & KITCHATINOV, L.L. 2006 Do mean-field dynamos in nonrotating turbulent shear-flows exist? *Astron. Nachr.* **327** (4), 298.
- SALHI, A. 2002 Similarities between rotation and stratification effects on homogeneous shear flow. *Theor. Comput. Fluid Dyn.* **15** (6), 339–358.
- SANADA, T. & SHANMUGASUNDARAM, V. 1992 Random sweeping effect in isotropic numerical turbulence. *Phys. Fluids A* **4** (6), 1245–1250.
- SESHASAYANAN, K. & ALEXAKIS, A. 2018 Condensates in rotating turbulent flows. *J. Fluid Mech.* **841**, 434–462.
- SINGH, N.K. & SRIDHAR, S. 2011 Transport coefficients for the shear dynamo problem at small Reynolds numbers. *Phys. Rev. E* **83** (5), 056309.
- SINGH, N.K. & SRIDHAR, S. 2017 Plane shearing waves of arbitrary form: exact solutions of the Navier–Stokes equations. *Eur. Phys. J. Plus* **132** (9), 403.
- SKOUTNEV, V., SQUIRE, J. & BHATTACHARJEE, A. 2022 On large-scale dynamos with stable stratification and the application to stellar radiative zones. *Mon. Notices Royal Astron. Soc.* **517** (1), 526–542.
- SOKOLOV, D.D. 1997 The disk dynamo with fluctuating spirality. *Astron. Rep.* **41** (1), 68–72.
- SQUIRE, J. & BHATTACHARJEE, A. 2015a Coherent nonhelical shear dynamos driven by magnetic fluctuations at low Reynolds numbers. *Astrophys. J.* **813** (1), 52.
- SQUIRE, J. & BHATTACHARJEE, A. 2015b Electromotive force due to magnetohydrodynamic fluctuations in sheared rotating turbulence. *Phys. Rev. E* **92** (5), 053101.
- SQUIRE, J. & BHATTACHARJEE, A. 2015c Generation of large-scale magnetic fields by small-scale dynamo in shear flows. *Phys. Rev. Lett.* **115** (17), 175003.
- SQUIRE, J. & BHATTACHARJEE, A. 2016 The magnetic shear-current effect: generation of large-scale magnetic fields by the small-scale dynamo. *J. Plasma Phys.* **82** (2), 535820201.
- SRIDHAR, S. & SINGH, N.K. 2010 The shear dynamo problem for small magnetic Reynolds numbers. *J. Fluid Mech.* **664**, 265–285.
- SRIDHAR, S. & SINGH, N.K. 2014 Large-scale dynamo action due to  $\alpha$  fluctuations in a linear shear flow. *Mon. Not. R. Astron. Soc.* **445** (4), 3770–3787.
- SRIDHAR, S. & SUBRAMANIAN, K. 2009a Nonperturbative quasilinear approach to the shear dynamo problem. *Phys. Rev. E* **80** (6), 066315.
- SRIDHAR, S. & SUBRAMANIAN, K. 2009b Shear dynamo problem: quasilinear kinematic theory. *Phys. Rev. E* **79** (4), 045305.
- STEENBECK, M., KRAUSE, F. & RÄDLER, K.-H. 1966 Berechnung der mittleren lorentz-feldstärke für ein elektrisch leitendes medium in turbulenter, durch coriolis-kräfte beeinflusster bewegung. *Z. Naturforsch. A* **21** (4), 369–376.
- SUR, S. & SUBRAMANIAN, K. 2009 Galactic dynamo action in presence of stochastic  $\alpha$  and shear. *Mon. Not. R. Astron. Soc.* **392** (1), L6–L10.
- TEED, R.J. & PROCTOR, M.R.E. 2016 Destruction of large-scale magnetic field in non-linear simulations of the shear dynamo. *Mon. Not. R. Astron. Soc.* **458** (3), 2885–2889.
- TRITTON, D.J. & DAVIES, P.A. 1985 Instabilities in geophysical fluid dynamics. In *Hydrodynamic Instabilities and the Transition to Turbulence* (ed. H. L. Swinney & J. P. Gollub), vol. 45, p. 229. Springer-Verlag.

- VISHNIAC, E.T. & BRANDENBURG, A. 1997 An incoherent  $\alpha$ - $\Omega$  dynamo in accretion disks. *Astrophys. J.* **475** (1), 263–274.
- WILKIN, S.L., BARENGHI, C.F. & SHUKUROV, A. 2007 Magnetic structures produced by the small-scale dynamo. *Phys. Rev. Lett.* **99**, 134501.
- YOUSEF, T.A., HEINEMANN, T., SCHEKOCIHIN, A.A., KLEORIN, N., ROGACHEVSKII, I., ISKAKOV, A.B., COWLEY, S.C. & MCWILLIAMS, J.C. 2008 Generation of magnetic field by combined action of turbulence and shear. *Phys. Rev. Lett.* **100** (18), 184501.
- ZEL'DOVICH, Y.B. 1956 A magnetic field in the two-dimensional motion of a conducting turbulent fluid. *Sov. Phys. JETP* **4**, 460.
- ZEMAN, O. 1994 A note on the spectra and decay of rotating homogeneous turbulence. *Phys. Fluids* **6** (10), 3221–3223.
- ZHOU, H. & BLACKMAN, E.G. 2021 On the shear-current effect: toward understanding why theories and simulations have mutually and separately conflicted. *Mon. Not. R. Astron. Soc.* **507** (4), 5732–5746.
- ZHOU, H., BLACKMAN, E.G. & CHAMANDY, L. 2018 Derivation and precision of mean field electrodynamics with mesoscale fluctuations. *J. Plasma Phys.* **84** (3), 735840302.